Structure of mitoribosome reveals mechanism of mRNA binding, tRNA interactions with L1 stalk, roles of cofactors and rRNA modifications

Vivek Singh[1,14], Yuzuru Itoh[1,2,14], Samuel Del'Olio[3,14], Asem Hassan[4,5,14], Andreas Naschberger[1,6], Rasmus Kock Flygaard[7], Yuko Nobe[8], Keiichi Izumikawa[9], Shintaro Aibara[10], Juni Andréll[11], Paul C Whitford[4,5], Antoni Barrientos[3,12,13], Masato Taoka[8], Alexey Amunts[1*]

[1] Science for Life Laboratory, Department of Biochemistry and Biophysics, Stockholm University, 17165 Solna, Sweden.
[2] Department of Biological Sciences, Graduate School of Science, University of Tokyo, 113-0033 Tokyo, Japan.
[3] Department of Molecular and Cellular Pharmacology, University of Miami Miller School of Medicine, Miami, FL 33136, United States.
[4] Department of Physics, Northeastern University, Boston, MA, 02115, United States.
[5] Center for Theoretical Biological Physics, Northeastern University, Boston, MA, 02115, United States.
[6] King Abdullah University of Science and Technology, Thuwal 23955, Saudi Arabia.
[7] Department of Molecular Biology and Genetics, Danish Research Institute of Translational Neuroscience - DANDRITE, Nordic EMBL Partnership for Molecular Medicine, Aarhus University, 8000 Aarhus C, Denmark.
[8] Department of Chemistry, Graduate School of Science, Tokyo Metropolitan University, Minami-osawa 1-1, Hachioji-shi, Tokyo 192-0397, Japan.
[9] Department of Biotechnology, Global innovation research institute, Tokyo University of Agriculture and Technology, Saiwai-cho 3-5-8, Fuchu-shi, Tokyo 183-8509, Japan.
[10] BioPharmaceuticals Research and Development, AstraZeneca, UK.
[11] Department of Medical Biochemistry and Biophysics, Karolinska Institutet, 17177, Stockholm, Sweden.
[12] Department of Neurology, University of Miami Miller School of Medicine, Miami, FL 33136, United States.
[13] Department of Biochemistry and Molecular Biology, University of Miami Miller School of Medicine, Miami, FL 33136, United States.
[14] These authors contributed equally

* correspondence: amunts@scilifelab.se

The mitoribosome translates mitochondrial mRNAs and regulates energy conversion that is a signature of aerobic life forms. We present a 2.2 Å resolution structure of human mitoribosome together with validated mitoribosomal RNA (rRNA) modifications, including aminoacylated CP-tRNA^{Val}. The structure shows how mitoribosomal proteins stabilise binding of mRNA and tRNA helping to align it in the decoding center, whereas the GDP-bound mS29 stabilizes intersubunit communication. Comparison between different states, with respect to tRNA position, allowed to characterize a non-canonical L1 stalk, and molecular dynamics simulations revealed how it facilitates tRNA transition in a way that does not require interactions with rRNA. We also report functionally important polyamines that are depleted when cells are subjected to an antibiotic treatment. The structural, biochemical, and computational data illuminate the principal functional components of the translation mechanism in mitochondria and provide the most complete description so far of the structure and function of the human mitoribosome.

The human mitoribosome translates at least 13 respiratory chain protein-coding mRNAs from the mitochondrial genome [1]. It consists of three rRNAs and at least 82 mitoribosomal proteins, 36 of which have no corresponding homologs in bacterial and cytosolic ribosomes. The mitochondrial rRNA is reduced compared to its bacterial counterpart (2,512 vs 4,568 nucleotides in *Escherichia coli*), $tRNA^{Val}$ has been incorporated as an additional constituent, and protein components are extended (~18,075 vs 7,536 residues in *E. coli*) [2]. The mitoribosomal proteins might have functional roles in mitochondria-specific aspects of translation, and therefore mutations in the corresponding genes result in cardio- and encephalomyopathies [3, 4]. However, due to the limited resolution and heterogeneity of the characterized complexes, the available models are currently incomplete, and many mitoribosomal protein key elements are described as unassigned densities [5, 6, 7, 8, 9, 10]. The existing models suggest that mitoribosomal proteins might play a role in binding mRNA, regulatory elements such as the L1 stalk are probably remodeled, and the specific mitoribosomal protein mS29, a putative GTPase is associated with inter-subunit communication. Yet, the lack of experimental data leaves open the questions of a functional involvement.

The mitochondrial rRNA is modified, and dedicated post-transcriptionally activated enzymes provide means for the regulation of gene expression and mitoribosome assembly [11]. Due to the central role of the human mitoribosome in cellular energy production, defects in rRNA modification result in fatal clinical syndromes from birth [12, 13]. Some of the bacterial counterpart modifying enzymes are missing from mitochondria, for example methyltransferases RlmA, RlmB, RmsE and pseudouridine synthase RluA, while other mitochondria-specific ones have evolved [14]. Therefore, rRNA modifications are different, and they have been identified by various experimental approaches [11, 15, 16, 17, 18, 19, 20, 21, 22, 23], furthermore recent structural studies visualized individual rRNA modifications on the mitoribosomal large (LSU) [24] and small (SSU) subunits [25, 26]. However, the entire set of modifications is yet to be quantitatively identified and visualized in the presence of bound ligands in order to enable a detailed examination of their roles. To date, the molecular mechanisms compensating for the lack of bacteria-like modifications remain unknown, as well as the modifications and the amino-acylation state of the structural $tRNA^{Val}$.

Mitoribosomes are also linked to age-related diseases that are associated with decline in mitochondrial function and biogenesis [27, 28, 29, 30]. Aging-related pathological changes can be inhibited by polyamine consumption [31, 32], which also has anti-inflammatory effects in mouse models *in vivo* [33]. Polyamines have been shown to be essential for mammalian cell differentiation and proliferation through their impact on translation dynamics [34, 35]. However, no polyamine biosynthetic pathways within mitochondria have been found, and their role in mitochondrial physiology remained unknown. Whether mitoribosomes might be related to these phenomena and associated with cellular senescence via polyamines needs to be explored.

To address these issues, we combined high resolution structural studies of mitoribosomal complexes with mass spectrometry based quantitative RNA analysis, biochemistry, and molecular dynamics simulations.

112 **Structure determination**

113 To produce a 2.2 Å overall resolution map of the mitoribosome, we collected five separate cryo-
114 EM datasets. Selected monosome particles were subjected to per-particle defocus, beam-tilt and
115 per-particle astigmatism correction, followed by Bayesian polishing [36, 37]. The data was then
116 sorted into 86 optics groups based on acquisition areas followed by beam-tilt, magnification
117 anisotropy and higher order aberration correction [38]. A final set of 509,691 particles yielded a 2.2
118 Å map. The local resolution was further improved by performing masked refinements around
119 different regions of the monosome. In addition, we obtained a 2.6 Å resolution map in the
120 presence of mRNA and three tRNAs in the classical state, and 3.0 Å resolution map with two
121 tRNAs in the hybrid state (Supplementary Figs. 1 and 2). The improved resolution allowed
122 building the most complete available model of the mitoribosome, including several key protein
123 extensions involved in tRNA binding (Fig. 1a). The presence of mRNA on the mitoribosome
124 further enabled modeling 32 of its residues, which we then used to trace mitochondria-specific
125 elements involved in mRNA binding and put the rRNA modifications in a functional context
126 (Fig. 1b).
127 To provide a description of the conformational changes associated with tRNA movement, we
128 next focused efforts on modelling the L1 stalk. Thus, we merged particles containing tRNA in
129 the E-site and through partial signal subtraction [39] and obtained a 2.9 Å resolution map of the
130 region, enabling model building of the L1 stalk (Supplementary Fig. 1). We then used this model
131 to perform molecular simulations of the complete ribosome with tRNAs.

132

133 **rRNA and protein modifications, aminoacylated tRNA^{Val}, polyamines**

134 On the rRNA level, the quality of the map allowed the modeling of 13 rRNA modifications, of
135 which 6 are mitochondria specific compared to *E. coli* [21]. All the rRNA modifications
136 were validated by a tailored quantitative method of Stable Isotope-Labeled riboNucleic Acid as
137 an internal Standard (SILNAS) [40] (Supplementary Figs. 3,4). The mitochondria specific
138 modifications include base methylations m^{5}U1076, m^{5}C1488 in the SSU; m^{1}A2617 in the LSU;
139 and m^{1}A9, m^{2}G10 and ψ39 in the tRNA^{Val} incorporated in the central protuberance (CP) [41, 42, 43]
140 (Fig. 1b). In the map, methylations of rRNA were identified by systematically examining the
141 density map for the presence of unmodeled densities continuous with the base or sugar moieties
142 of rRNA residues (Fig. 2). Identity of the two high-occupancy pseudo-uridines was established
143 based on the presence of a structured water molecule within hydrogen-bonding distance from the
144 N5 atom.

145 The tRNA^{Val} modifications are consistent with the previous mass-spectrometry data on isolated
146 mitochondrial tRNAs from a general pool [44] (Fig. 3). The density further revealed that the
147 tRNA^{Val} incorporated in the CP is amino acylated (Fig. 2a). In the structure, ψ39 of tRNA^{Val}
148 contributes to the conformation of the anticodon arm, which contacts uL18m, mL38, mL40 and
149 mL48 (Fig. 3a). In addition, two methylated residues, m^{1}A and m^{2}G, are observed at the
150 positions 9 and 10, respectively in the D arm (Fig. 3a). m^{1}A9 is stacked between G45 and A46

151 and forms a base triple with the second base pair (C11:G24) of the D stem. On the other hand,
152 m^2G10 is stacked between C11 and A26 and forms the first base pair (m^2G10:C25) of the stem,
153 which further interacts with G45 to be a base triple. These methylations facilitate the stacking
154 and hydrogen bonds among bases, and thereby contribute to the conformation of the D arm,
155 which contacts uL18m and mL38 (Fig. 3a-c). The terminal A76 has a base-specific interaction
156 with Q175 of mL46 and together with Valine is stacked with F165 and F215 (Fig. 3d).
157 A notable feature of the cryo-EM map is the presence of continuous tubular densities associated
158 with rRNA that we assigned as polyamines, justified by the electrostatic and hydrogen-bonding
159 interactions at the amine groups (Supplementary Fig. 5). Thus, in addition to a previously
160 assigned spermine (SPM) [45], we detected one triamine spermidine (SPD) in the SSU, and a
161 diamine putrescine (PUT) and three SPDs in the LSU. The identified polyamines are bound to
162 negatively charged rRNA where mitochondria specific changes occur, providing required
163 structural support (Fig. 4; Supplementary Fig. 5). For example, SPD3301 in the LSU fills the
164 formed space of a shortened mitoribosomal protein uL2m, which has undergone reduction in the
165 human mitoribosome. SPD3303 is tethered to uL3m, where a bacterial counterpart has a
166 signature Q150 methylation, therefore replacing the post-translational modification. The PUT is
167 found in the exit tunnel upper region of uL22m hairpin.

168 Finally, the model contains six protein modifications; three iron-sulfur clusters, one of which is
169 coordinated by uL10m and mL66 and reported here for the first time, and a molecule of
170 nicotinamide adenosine dinucleotide (NAD) reported previously [26, 45, 46] (Fig. 1b, Supplementary
171 Table 1). We also identified a disulfide bond in one of the two redox active cysteine pairs in
172 mS37 (CHCHD1) (Fig. 2) that is oxidized in the intermembrane space during mitochondrial
173 import, representing a quality control mechanism [47].

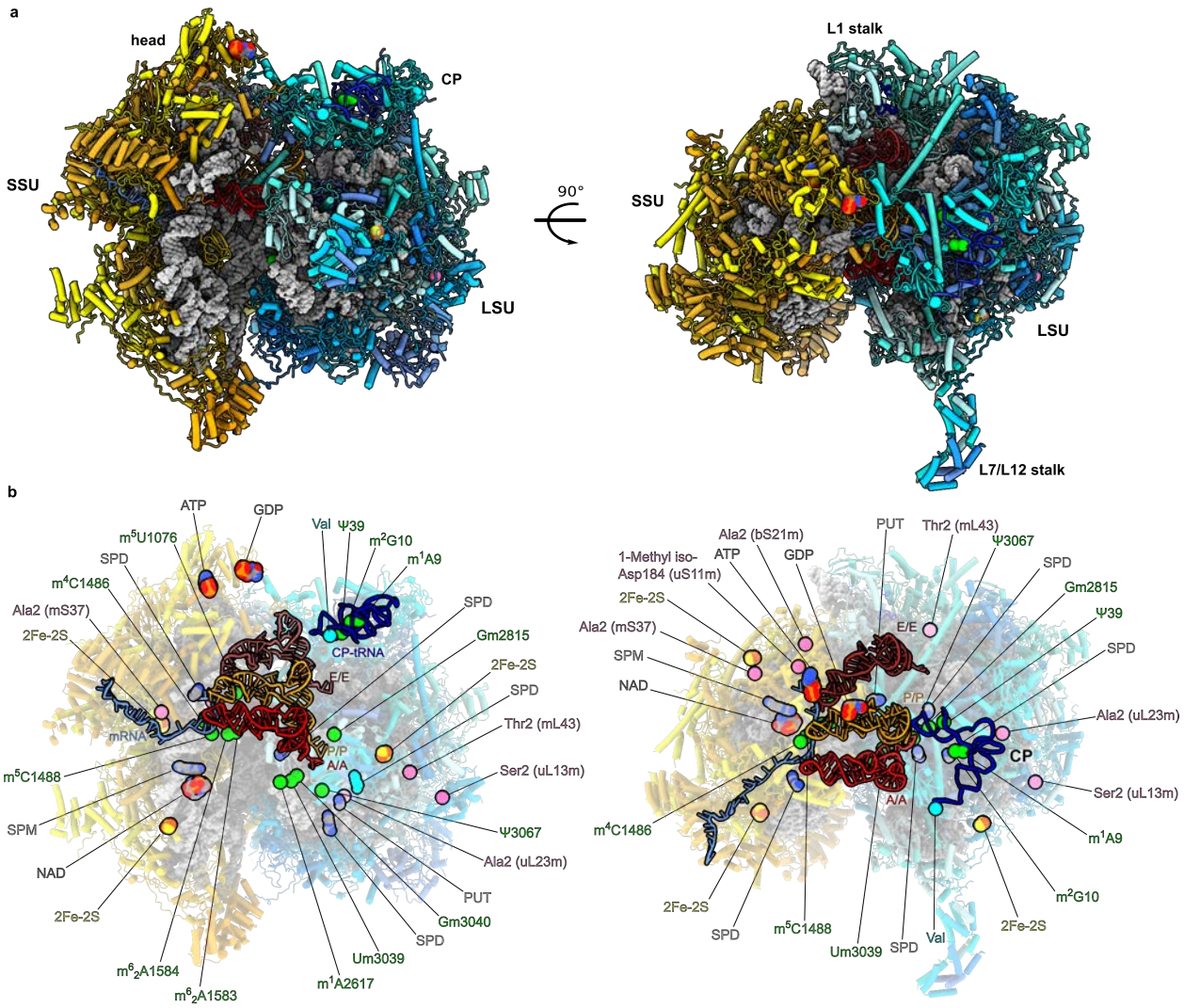

Fig. 1: Structure of the human mitoribosome. a, Overview of the 2.2 Å resolution model with mRNA and tRNAs. Proteins are shown as cartoons colored in blue for the LSU and yellow for the SSU. The rRNA is shown as grey surface. Newly identified features are shown as spheres. **b,** The newly identified cofactors and modifications are indicated against background of translucent rRNA and proteins with tRNAs and mRNA shown in cartoon. We observe 13 rRNA modifications (green), 6 protein modifications (pink), 3 iron-sulfur clusters (red-yellow), guanosine diphosphate (GDP), adenosine triphosphate (ATP), NAD, SPM, 4 SPDs and PUT.

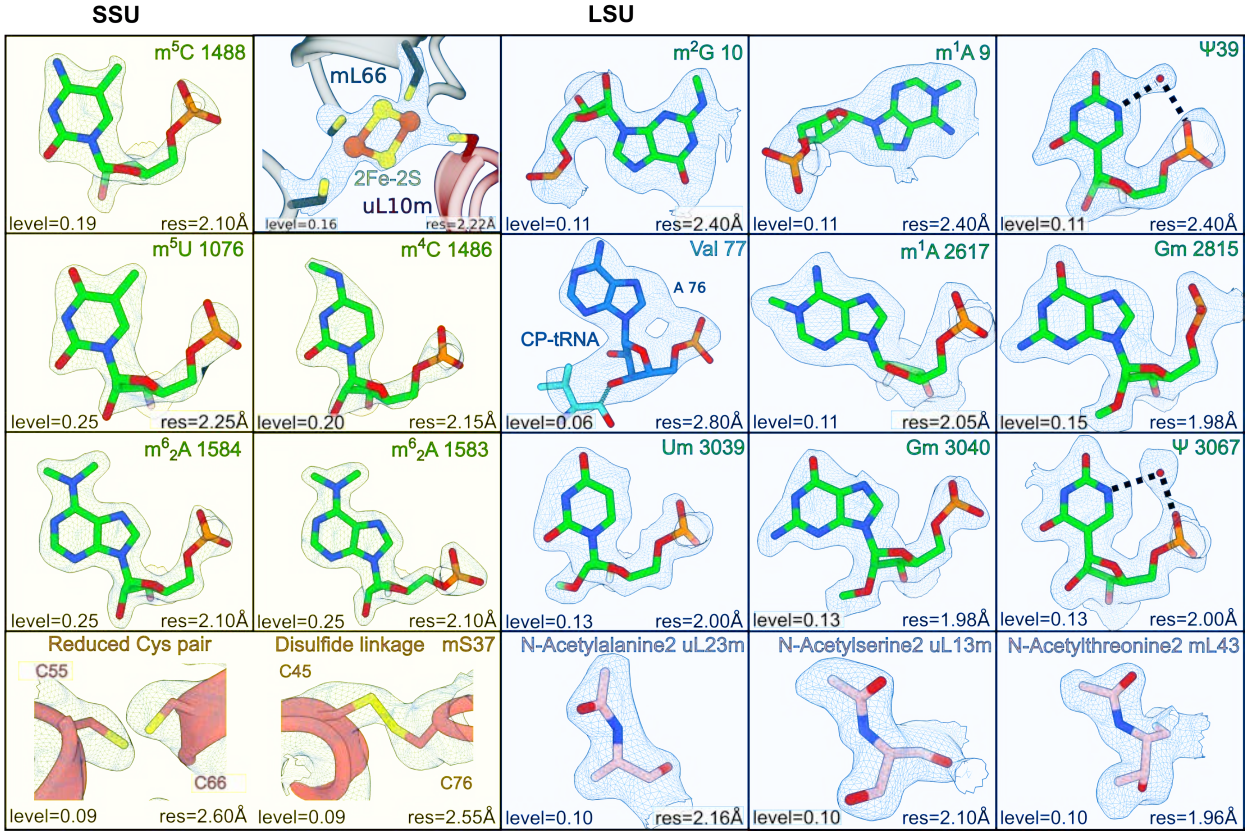

Fig. 2: High resolution features. Modified rRNA residues and disulfide-linked or reduced cysteine residues of mS37 in the SSU (yellow background). Modified rRNA and protein residues, and 2Fe-2S cluster in the LSU (cyan background). Their corresponding densities in the 2.2 Å map are shown as mesh at indicated threshold (bottom left) and local resolution (bottom right) levels.

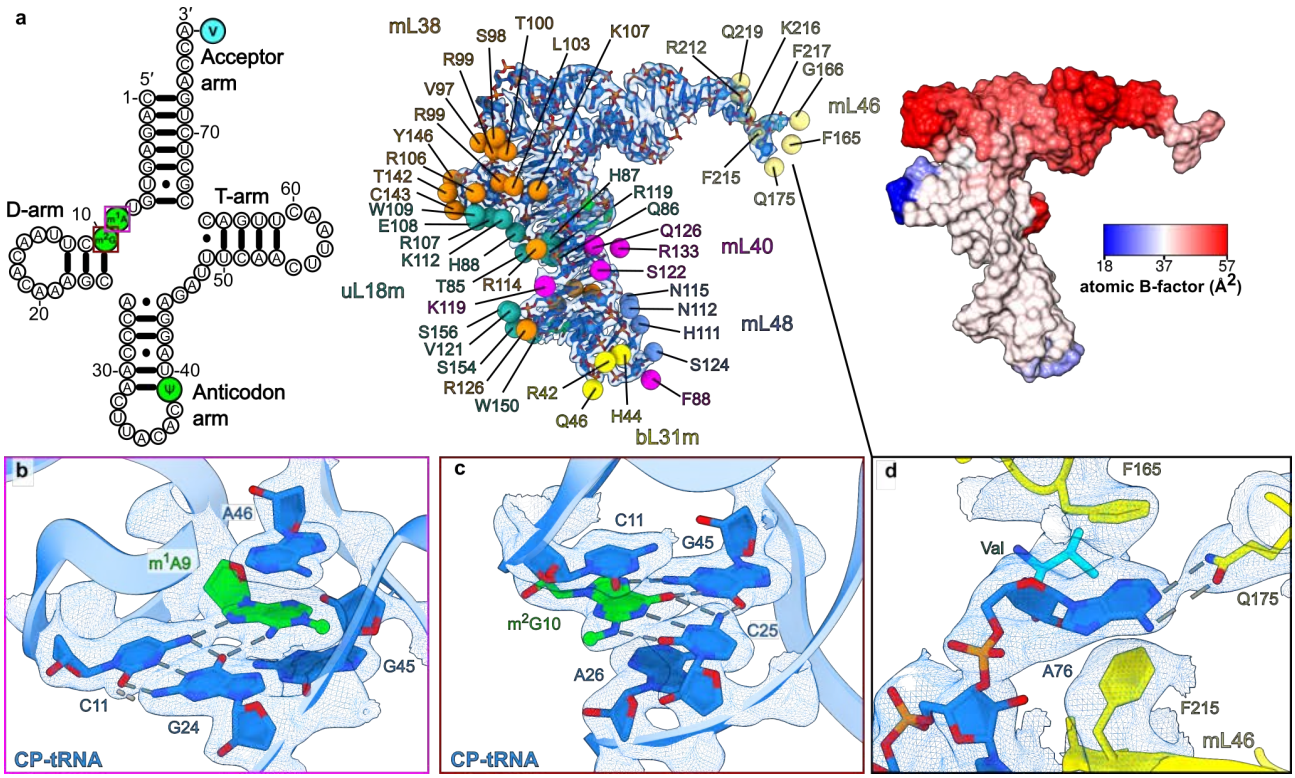

Fig. 3: Interactions and post-transcriptional modifications in CP-tRNA of the mitoribosome. a, CP-tRNA^{Val} (left to right) secondary structure diagram with modified nucleotides (green) and valine (cyan) highlighted, protein-contact map, *B*-factor representation. **b,c,** Interactions of the modified m^{1}A9 and m^{2}G10 nucleotides of CP-tRNA^{Val}. **d,** Interactions of A76 and V77 of CP-tRNA^{Val} with mL46. The cryo-EM density map is displayed for panels b-d (consensus map) as blue mesh. Panels (b) and (c) are related to panel (a) on the left by colored boxes.

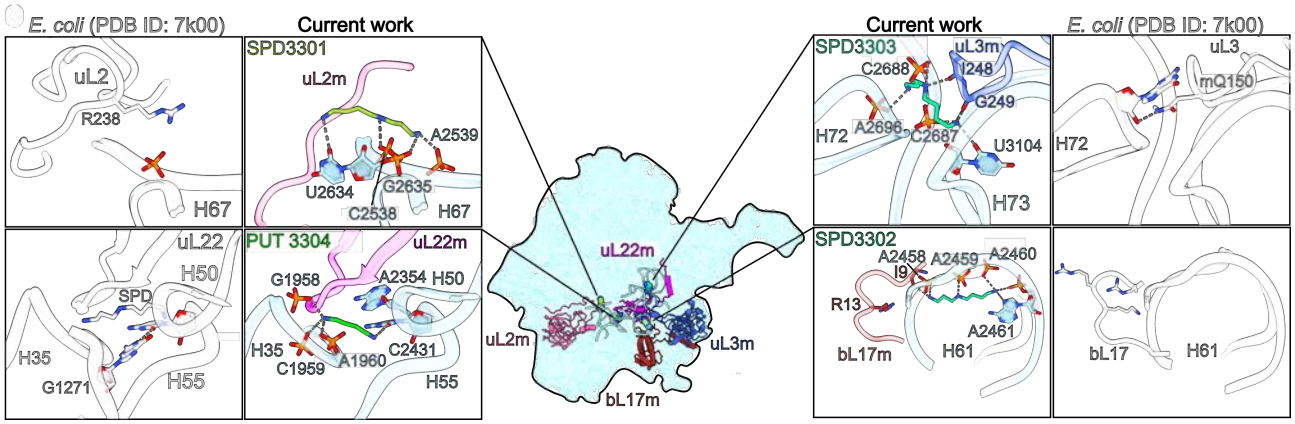

Fig. 4: Polyamines functionally compensate for rRNA and protein alterations. Central inset shows positions of polyamines and interacting rRNA and proteins in the LSU. For each polyamine, its environment and interacting partners are shown in zoom-in panels with *E. coli* counterparts [48] (white) for comparison.

202 **Initial binding of mRNA involves Y-N-C-Y motif coevolved with mS39**

203 The modulation of a stable mitoribosomal complex allowed us to resolve the mRNA path and
204 investigate mitoribosome-specific components involved in mRNA recognition (Fig. 5,
205 Supplementary Fig. 6, Supplementary Video 1). It engages seven helical repeats of mS39 with
206 specific contacts within a prominent positively charged groove (Fig. 5a). Particularly, a
207 pyrimidine ring of the mRNA nucleotide in position 25 is stacked between H489 and R524 and
208 interacts with S490 of mS39 (Fig. 5a,b). Hydrogen bonding between the side chain of R377 of
209 mS39 and nucleotide 27 favors cytosine over uracil because the protonated N3 of a uracil would
210 partially clash with the protonated Nη of R377. R343 of mS39 forms a hydrogen bond with the
211 pyrimidine ring of nucleotide 28. Thus, the structure reveals a binding motif: 25 pyrimidine (Y),
212 27 cytosine (C), 28 pyrimidine (Y) (Fig. 5a,b). Bioinformatic analysis showed that the Y-N-C-Y
213 motif is enriched in mitochondria and distributed over the entire length of each of the 12 open
214 reading frames in the guanine-rich heavy DNA strand, suggesting a co-evolution of the
215 mitochondrial DNA and the mitoribosome (Fig. 5c, Supplementary Fig. 7). The only mammalian
216 protein-coding gene with a reduced frequency of the Y-N-C-Y motif is the *MT-ND6* that is on
217 the light strand and codes for an 18-kDa subunit of complex I. The expression of the ND6
218 mRNA is unique, as it requires an auxiliary factor FASTK to generate the mature form,
219 suggesting a dedicated regulatory mechanism [49].

220 The most 5' contact between mRNA and mS39 is ~50 Å from the channel entrance, and by
221 following the mRNA density toward the decoding center, we identified six specific
222 mitoribosomal proteins that are important for mRNA recruitment, channel opening, and precise
223 alignment of the message for translation in the decoding center. In our structure, the Y-N-C-Y
224 motif forms a ~100° turn (kink-1) in the mRNA midway through mS39 (Fig. 5a and
225 Supplementary Video 1). After the kink, the N-terminal mitochondria-specific extension of
226 uS5m supports the path of mRNA over a distance of ~60 Å, involving a unique N-terminal
227 polybasic stretch of 14 residues 111-124 (KKGRGKRTKKKKRK) together with R237 and
228 K239 (Fig. 5d, Supplementary Video 1, Supplementary Fig. 6). From the side of the SSU head,
229 mS35 provides potential stabilizing electrostatic interactions to mRNA with N-terminal residues
230 K46 and K49 (Fig. 5e,f). This mitochondria-specific extension of uS5m structurally replaces
231 bacterial bS4 and uS3-CTD that interact with mRNA (Supplementary Fig. 6) and confer RNA
232 helicase activity on the bacterial ribosome [50]. Just before the channel entry, the binding of
233 mRNA induces a conformational change of the N-terminal extension of uS9m that contacts the
234 mRNA nucleotide at position 15 via the backbone of V55 (Fig. 5e,g; Supplementary Video 1),
235 which in the absence of mRNA blocks the entrance to the decoding center [51]. Thus, uS9m exists
236 in a closed conformation in the absence of mRNA, and upon mRNA threading, a conformational
237 change in uS9m allows the passage (Fig 5h).

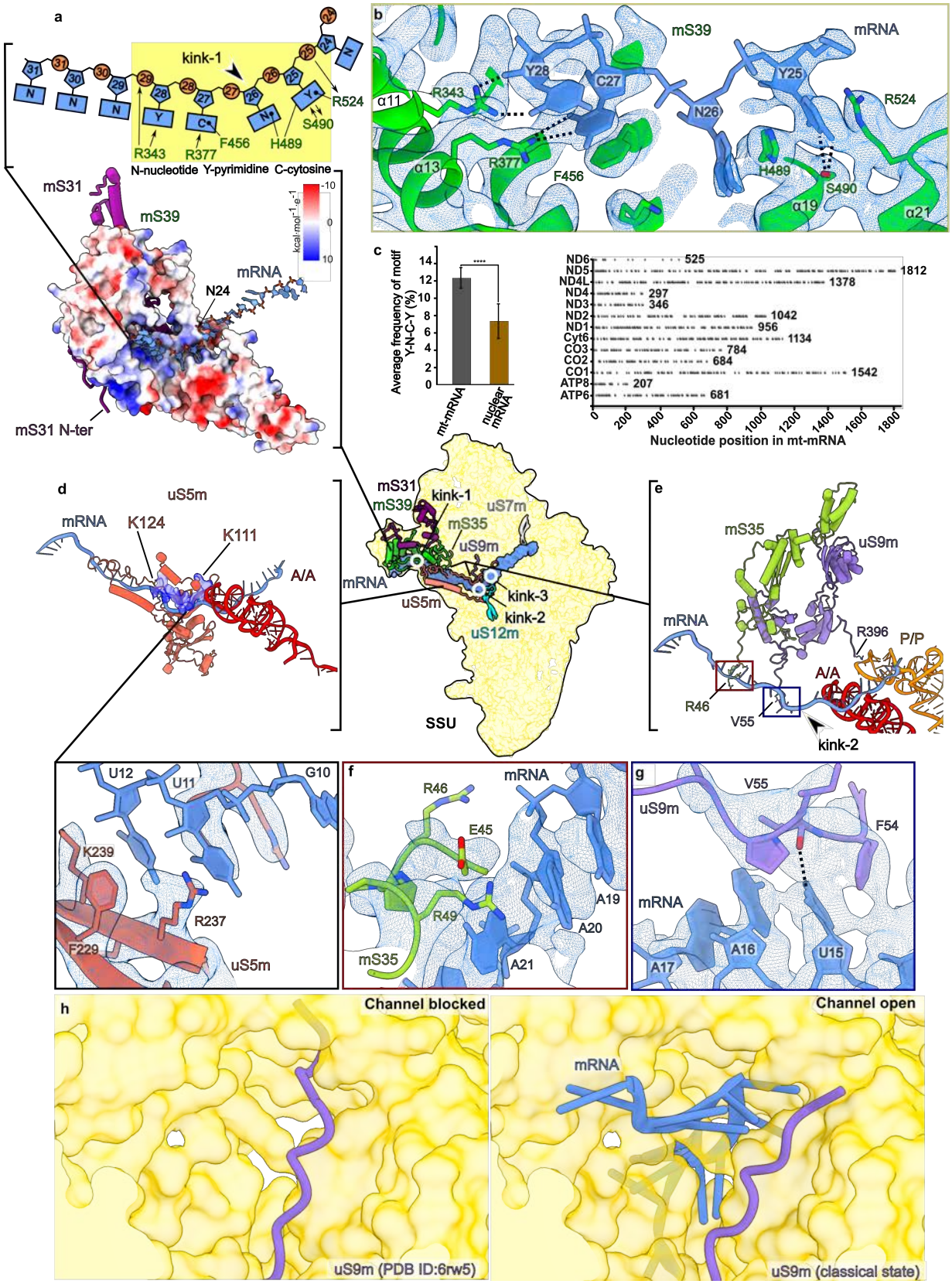

238

239 **Fig. 5: Specific protein elements involved in mRNA binding.**

240 **a,** Electrostatic coulomb potential surface representation of the model shows a positively charged
241 groove (blue) on mS39 that accommodates the mRNA. N-terminal loop of mS31 interacts with
242 mS39. Y-N-C-Y motif and its interactions with mS39 residues are depicted as a schematic.
243 Position of kink-2 is marked. **b,** Interactions of the Y-N-C-Y motif with mS39 and density map
244 (mesh). Protein mS31 has been removed for clarity. **c,** Average percentage frequency of Y-N-C-
245 Y motif (left) with +/- standard deviation for mitochondrial mRNAs (excluding ND6; dark grey
246 bar) and nuclear mRNA (brown bar). P-value (<0.0001) calculated by Welch's unpaired t-test.
247 Positions of the Y-N-C-Y motif in the mt-mRNAs are shown as discs (right) to depict its
248 distribution along the mt-mRNA sequences. The total number of residues for each mt-mRNA is
249 indicated. **d,** Overview of uS5m showing a region of contact with mRNA. The polybasic stretch
250 111-124 along the mRNA is colored by electrostatic potential. Interacting residues between
251 uS5m and mRNA are shown with the local density map. **e,** Interactions of mS35 and uS9m with
252 mRNA at the channel entry and the P-site. **f,** R46 and R48 of mS35 potentially interact with the
253 mRNA backbone, and the density suggests flexibility of the side-chains. **g,** uS9m forms stacking
254 and hydrogen bonding interactions with mRNA position 15 via F54 and V55, respectively. **h,**
255 uS9m N-terminus (purple cartoon) adopts alternative conformations that result in mRNA channel
256 blocked or open states regulating mRNA access to the SSU (gold surface).
257
258 **mL40 N-terminal tail stabilizes the A- and P-site tRNAs and decoding interactions**

259 We then examined the role of mitoribosomal proteins in the mRNA alignment. The structure
260 shows that to enter the SSU channel, the mRNA must be kinked again (kink-2), and in the A-site
261 the nucleotide at position 9 is stabilized by uS12m (Supplementary Fig. 8). Here, a conserved
262 K72 side chain forms a salt bridge with the phosphate of nucleotide 9 (last nucleotide in the A-
263 site codon). At the same time, *cis*-proline P73 (Supplementary Fig. 8) coordinates two potassium
264 ions, one of which directly coordinates 2´O of nucleotide 9 (Supplementary Fig. 8,
265 Supplementary Video 1) and stabilizes the decoding center. The densities identified as two
266 potassium ions have been observed previously, but modeled as Mg^{2+} (PDB 4V51) [52] or waters
267 (PDB 7K00) [48, 52]. However, they have been experimentally identified as K^{+} by long wavelength
268 X-ray diffraction analysis (PDB 6QNR) [53], which agrees with our assignment (Supplementary
269 Fig. 8).

270 Next, between the A- and P-site, the map reveals a third kink in the mRNA (kink-3), which is co-
271 localized with a 35-Å long density extending from the CP in between the two tRNAs (Fig. 6a,
272 Supplementary Fig. 9a) that could not be previously interpreted. We identified it as a positively
273 charged N-terminus of mL40 with the terminal backbone amino group of S47 forming a salt
274 bridge with the backbone phosphate of the mRNA at position 7 in the A-site (Fig. 6a,
275 Supplementary Fig. 9b), and the interaction is further stabilized via a magnesium ion coordinated
276 by the phosphate of G1485. In addition, the hydroxyl group of S47 interacts with the mRNA
277 nucleotide base at position 6 in the P-site (Fig. 6a, Supplementary Video 1), although the
278 contacts are likely to be flexible. Moreover, the base orientation allows any nucleotide to interact
279 with S47 (Supplementary Fig. 9c). The concept is analogous to the cytosolic ribosome that

engages uS19 for tRNA stabilization and mRNA interactions in the decoding center [54] (Fig. 6b). The presence of four lysine residues 52-55 (Fig. 6a, Supplementary Fig. 9b), might suggest that mL40 contributes to balancing the charge between the A- and P-tRNAs. Together with R51, which forms salt bridges with A1560 and C1561 in h44, the positively charged patch compensates for the negative RNA charges accumulated in that region (Fig. 6a, Supplementary Fig. 9b, Supplementary Video 1). Further in the P-site, we observe a well-resolved density showing the conserved C-terminal R396 of uS9m interacting with the anticodon loop of the P-site tRNA (Supplementary Fig. 9d). Finally, in the E-site, uS7m residues G164-165 further contribute to mRNA stabilization (Supplementary Fig. 9e). Thus, mitoribosomal proteins play a role in mRNA binding.

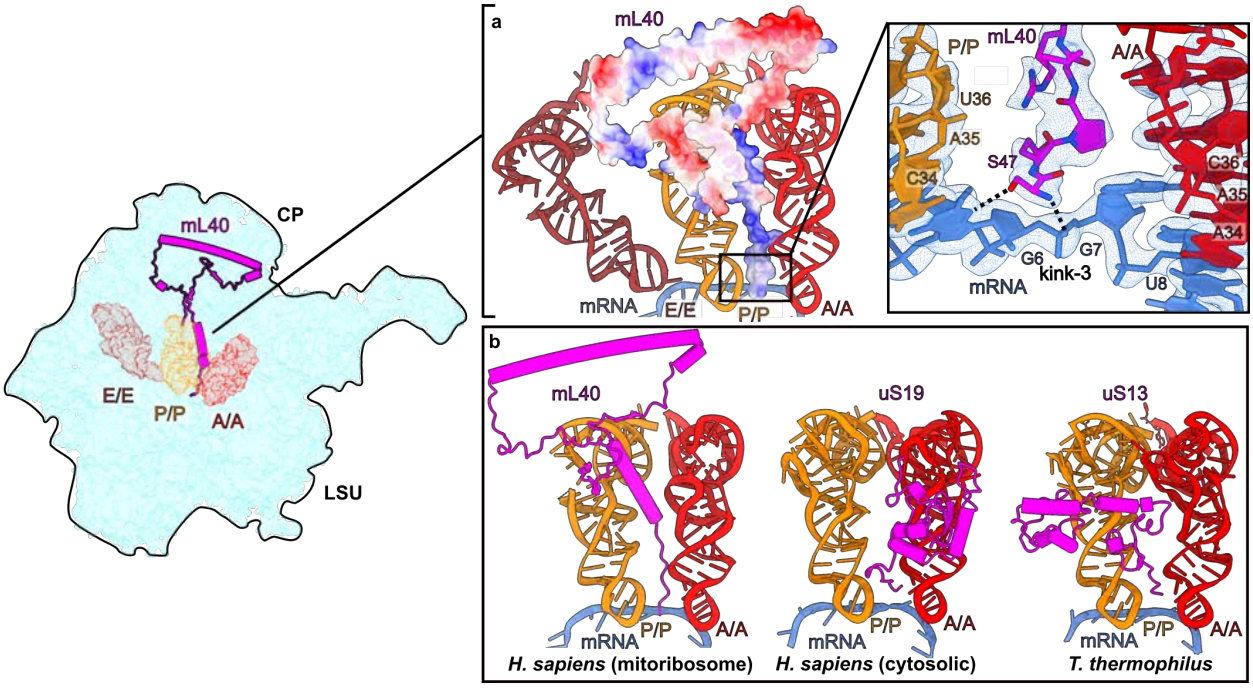

Fig. 6: Analysis of mRNA binding in tRNA sites. a, Interactions of mL40 (shown with electrostatic potential of the model) with mRNA between A/A- and P/P-tRNAs. Hydrogen bonds G6 base and G7 phosphate are shown as dashed lines. **b,** Comparison of mL40-tRNA interaction (left) with those of uS19 (middle) and uS13 (right) in human cytosolic [54] and *T. thermophilus* ribosome [52], respectively.

mRNA alignment in the decoding center and rRNA modifications

In the decoding center, the universally conserved G902 is in *anti* conformation, while A1557 and A1558 are flipped out from h44 to interact with the A-site codon:anti-codon helix in the canonical manner [55, 56] (Supplementary Fig. 10). A well-resolved density, combined with the mass-spectrometry SILNAS [40, 57, 58] approach further allowed us to validate the complete set of the rRNA modifications, including six mitochondria specific, and propose a role in stabilizing the decoding center (Fig. 5, Supplementary Figs. 4 and 5). Close to the decoding center, the residue G899 was recently shown to interact with streptomycin in human mtSSU [45]. Its

305 methylated to m^7G527 in *E.coli* (Supplementary Fig. 10) and this modification partly contributes
306 to streptomycin sensitivity [59]. In the P-site, two base-methylated nucleotides m^4C1486 and
307 m^5C1488 flank the base triple C1487:A1564:U1563 by stabilizing the stacking interactions (Fig.
308 5a,b). The orientation of N^4-methylated m^4C1486 towards mRNA is conserved with respect to *E.*
309 *coli*, where the corresponding residue is also 2'-O methylated ($m^4Cm1402$) (Supplementary Fig.
310 10). m^4C1486 together with C1487 interacts with the phosphate group of the last nucleotide in
311 the P-site mRNA codon via hydrogen bonds (Fig. 5a,b). Further, phosphate group of m^4C1486
312 coordinates a magnesium ion, which stabilizes a conserved kink of the mRNA between A- and
313 P-sites (Fig. 7a). In contrast to the *E. coli* P-site, U1563 does not have an N^3-methylation
314 (m^3U1498 in *E. coli*) (Supplementary Fig. 10). This lack of N^3-methylation allows U1563
315 together with C1487 to form a water mediated interaction with the P-site codon (Fig. 7a,b).
316 Further, the conserved dimethylated residues, $m^6{}_2A1583$ and $m^6{}_2A1584$ orient the nucleotide
317 U1563 such that the ribose of U1563 forms a hydrogen bond to a phosphate group of the second
318 nucleotide in the P-site mRNA codon, while the phosphate of U1563 forms a hydrogen bond
319 with the ribose on the first codon nucleotide (Fig. 7b). The two dimethylated nucleotides
320 facilitate A1080 positioning for the 2′-OH to hydrogen bond with N3 of m^5U1076. This together
321 with methylation of m^5U1076 contributes to the stability of h24 loop that interacts with the P-
322 tRNA anticodon stem at position 38 via A1078 (Fig. 7a,b).

323 In the A-loop of H92, there are two 2′-O-methyl modified nucleotides Um3039 and Gm3040.
324 The 2′-O-methyl of Um3039 sterically positions the bases of Gm3040 and U3041 to form
325 interactions with the nucleotides C75 and C74 of the A-tRNA, respectively (Fig. 7c,d). The 2′-O-
326 methyl of Gm3040 present in the cytosolic but not bacterial ribosome and interacts with the base
327 of A3069 to stabilize the conformation of Gm3040. Furthermore, the bacterial counterpart rRNA
328 that interacts with A-tRNA (C75) is G:C, whereas in our structure it's A:U (3069:2994) that is
329 less stable, and thus stabilized by the mitochondria-specific methylation of Gm3040 and base-
330 pairing interactions with ψ3067 (Fig. 7d). In the LSU, mitochondria-specific m^1A2617 positions
331 U2614 into a wedged interaction (Fig. 7e). Surprisingly, there is only weak sugar puckering for
332 m^1A2617 (Fig. 2a). It bears a partial positive charge at N1 and interacts with U2649 of H61. The
333 interactions mediated by m^1A2617 potentially contribute to the structuring of H71 loop that
334 participates in an intersubunit bridge shares an interface with the A-loop (Fig. 7e). The
335 universally conserved Gm2815 in the P-loop forms Watson-Crick base pairing with C75 of P/P-
336 tRNA, similar to the interactions of Gm3040 of the A-loop (Fig. 7f).

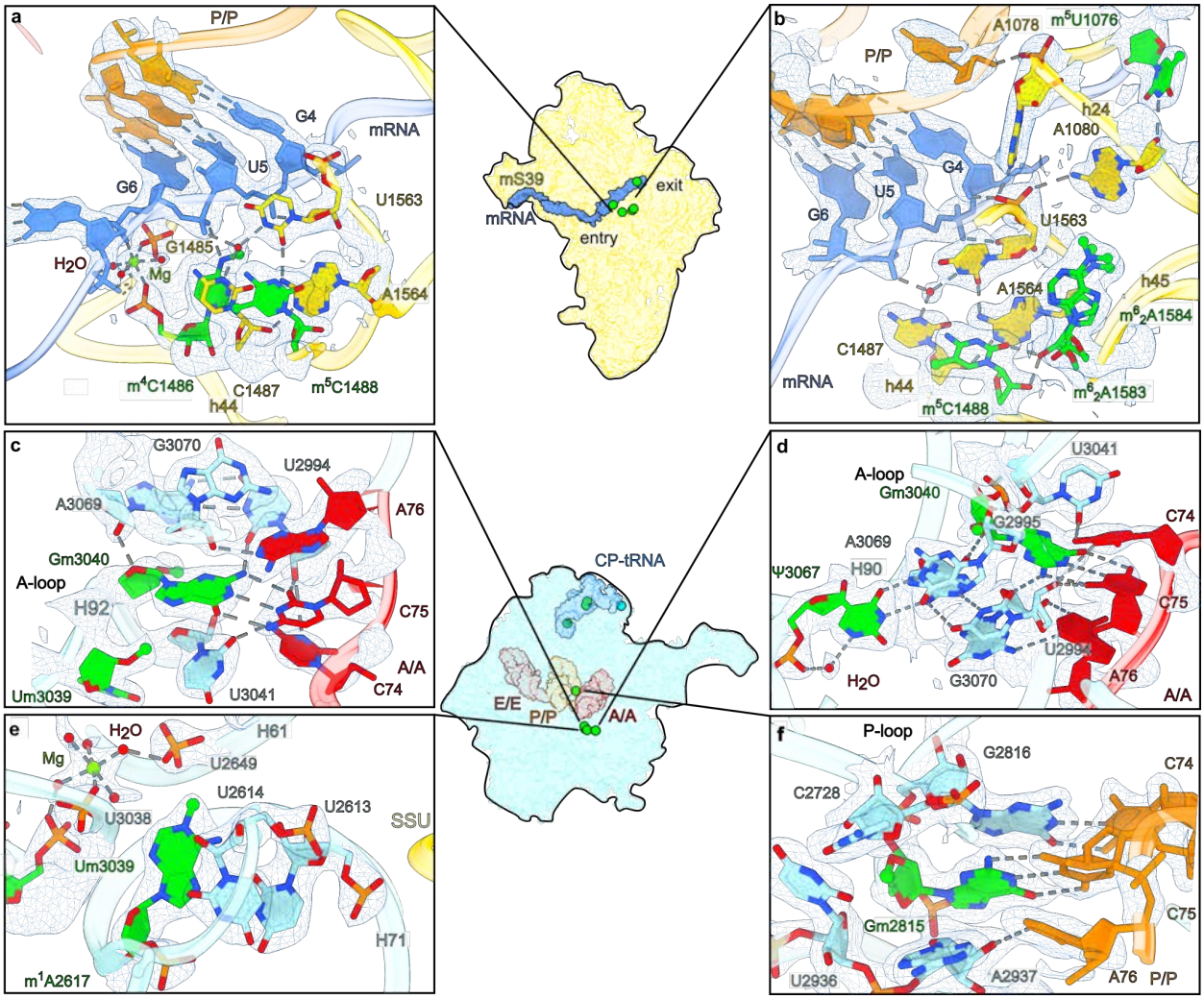

Fig. 7: Post-transcriptional modifications in functional centers of the mitoribosome. **a,** Base-methylated m^4C1486 and m^5C1488 and the interactions at the P-site mRNA codon. **b,** The dimethylated $m^6{}_2A1583$, $m^6{}_2A1584$ and base-methylated m^51076 facilitate interactions with mRNA codon and P-tRNA. **c,** 2′-*O*-methyl modified Um3039 and Gm3040 lead to interactions with A-tRNA. **d,** Gm3040 and Ψ3067 contribute to the interface with the A-tRNA. **e,** m^1A2617 contributes to a stabilization of inter-subunit bridge and the A-loop. **f,** Gm2815 base-pairs with P-tRNA. Cryo-EM density map (A/A P/P E/E state) is displayed as a blue mesh.

Structure of the mitoribosomal L1 stalk reveals its unique protein features

To investigate whether mitoribosomal proteins might also have influence on tRNA rearrangement in the E-site, we aimed to perform molecular simulations of the mitochondrial L1 stalk. Therefore, we modeled the complete structure of the L1 stalk, which relies on mitochondria specific protein elements. In the structure, the E-tRNA is stabilized via mitochondria-specific protein elements of the C-terminal domain of uL9m and 33-residue N-terminal extension of uL1m (Fig. 8a,b). The orientation of the uL9m C-terminal domain adopts a

353 previously unseen folded conformation involving a ~75° rotation towards the E-tRNA (Fig. 8c).
354 This unexpected conformational difference is facilitated by the C-terminal helix in the extension
355 that reaches and contacts the non-base-pairing part and the distal short hairpin of the rRNA H76
356 (Fig. 8d). The resulting projection of uL9m towards the ribosomal core reduces the distance
357 between the central helix and the C-terminus of uL1m from ~70 to only ~30 Å. This distance is
358 spanned by the uL1m mitochondria-specific extension that forms direct contacts with the central
359 helix of uL9m (Fig. 8d-f). Therefore, our model of the L1 stalk establishes a tertiary
360 mitoribosomal complex uL9m:uL1m:rRNA-H76, where uL9m acquires a new functional role.
361 From the opposite side, the mitochondria-specific mL64 approaches the T-arm through its long
362 C-terminal helix extending to the tRNA binding sites.

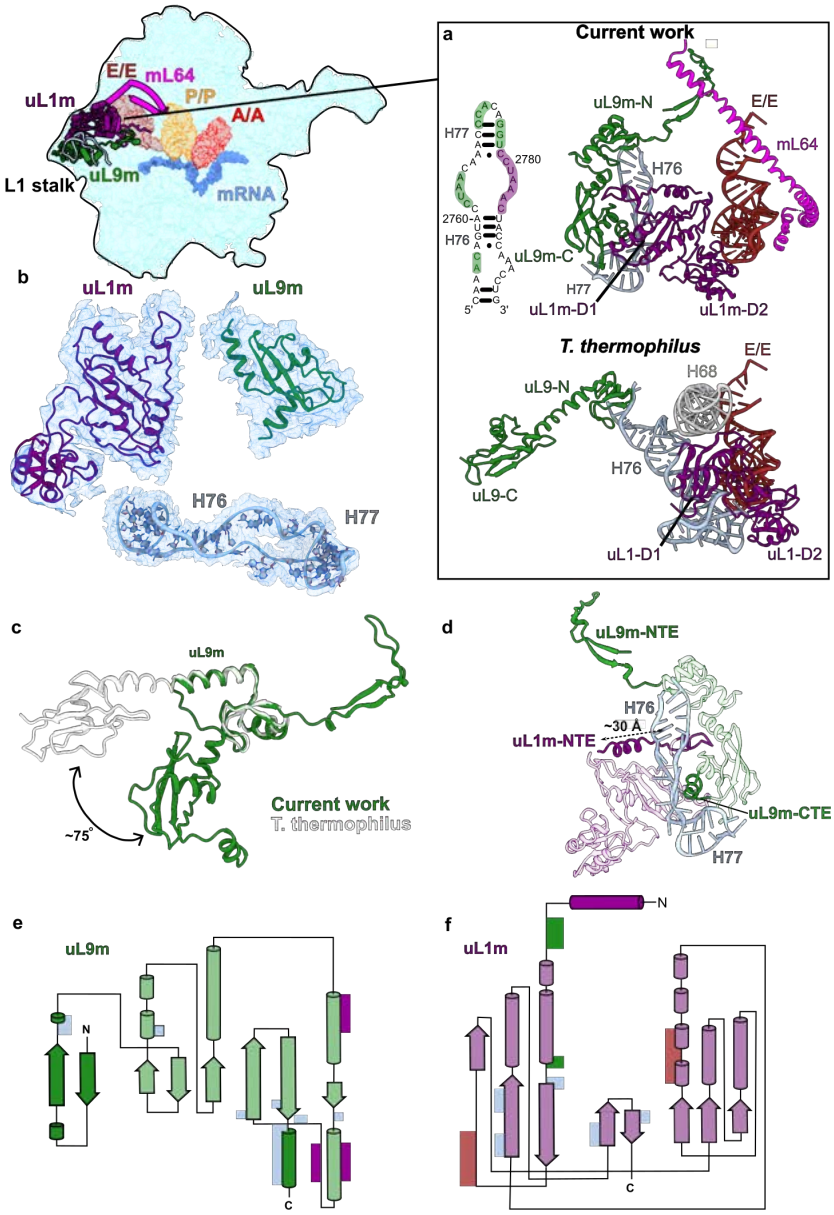

363
364 **Fig. 8: Structural features of the L1 stalk and interactions with tRNA.**

365 **a,** The L1 stalk components uL9m (green), uL1m (purple) rRNA helix H76-77 (residues 2757-
366 2790, light blue), as well as mL64 (magenta) interact with E/E-tRNA. The structure and
367 interactions are different from *T. thermophilus* (PDB ID: 4V51) [52] **b,** Components of the L1 stalk
368 modeled into their respective densities (shown as mesh). **c,** Comparison of uL9m conformation
369 with that of *T. thermophilus* uL9 (white PDB ID 4V51). **d,** Model of uL1m stalk with uL9m in
370 green and uL1m in purple, highlighting mitochondria-specific protein elements. **e,** 2D diagram of
371 uL9m showing interactions with E/E-tRNA (brown bars), rRNA (light-blue bars), uL1m (dark-
372 blue bars). Conserved regions are shown in light and mitochondria-specific in dark colors. **f,** 2D
373 diagram of uL1m color-coded as in panel d.
374

375 **Recognition of tRNA by the L1 stalk and intersubunit communication**

376 We next used an all-atom structure-based model [60, 61] to simulate hundreds of transitions of the
377 tRNA from the P site to P/E state (Fig. 9a,b; Supplementary Video 2). To isolate the influence of
378 uL1m and mL64, we compared the dynamics with four variants of the model (Fig. 9c; see
379 Methods): 1) baseline model; 2) truncated mL64 (ΔmL64) with C-terminal region starting with
380 Q112 being removed to prevent steric interactions between mL64 and EE-tRNA without
381 disturbing the rest of the protein.; 3) modified uL1m (ΔuL1m) where stabilizing interactions
382 between uL1m and P-site-tRNA are scaled down compared to the baseline model (values
383 available in methods); 4) both ΔmL64 and ΔuL1m modifications are included (see methods
384 section for details of the models). Using these models, we simulated 1066 spontaneous (non-
385 targeted) transitions between the classical (A/A P/P) and hybrid (A/P P/E) states, which include a
386 ~40 Å displacement of the P-tRNA and spontaneous rotation of the SSU (Supplementary Video
387 2). A mechanistic insight from these calculations is that mL64 imposes strict limits on the
388 pathways that are accessible to tRNA, which thereby favors a specific sequence of
389 conformational substeps during P/E formation (Fig. 9d-g). As a result, mL64 ensures that the
390 tRNA is properly positioned and may reliably engage uL1m as the tRNA approaches the E site.
391 The structure also shows that due to the different type of tRNA binding, no base pairs are formed
392 between the E/E-tRNA and mRNA, unlike those found in bacteria [62] (Supplementary Fig. 9e).
393 Instead, the protein uS7m undergoes a conformational change in which residues G164-165
394 directly contact the mRNA and stabilize its binding (Supplementary Fig. 9e, Supplementary
395 Video 1). Thus, upon each translation step, a tRNA is recognized in the E-site and escorted from
396 the mitoribosome without involving rRNA, which is strikingly different from bacterial and
397 cytosolic counterparts.

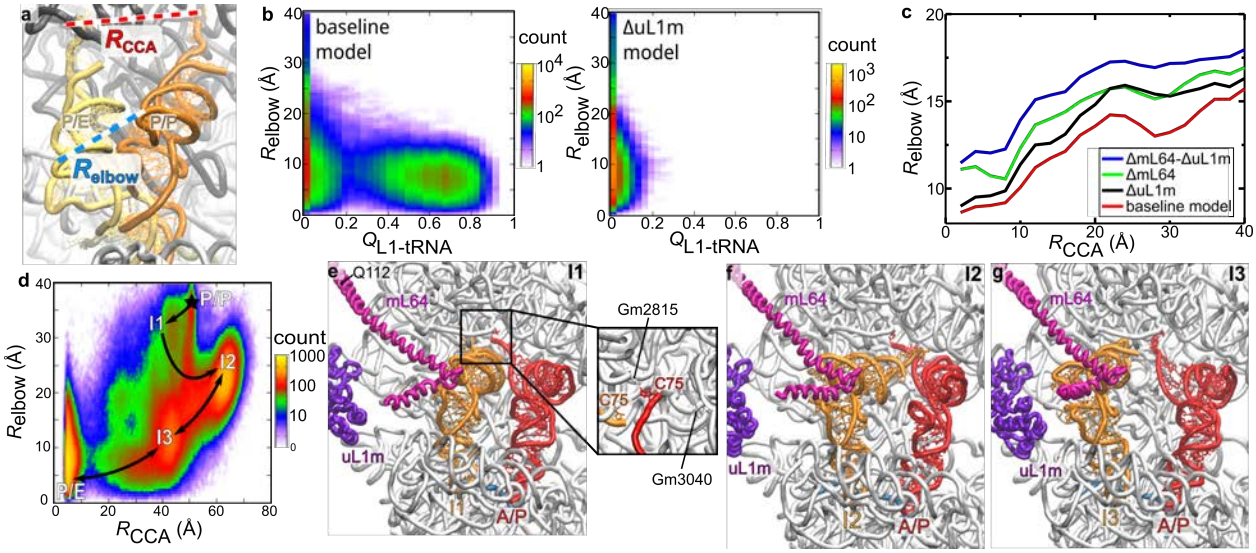

Fig. 9: Simulations of P/E formation reveal the influence of mitochondria-specific proteins. **a,** Distances R_{elbow} and R_{CCA} are used to describe the position of the tRNA during P/E formation. **b,** Probability distribution as a function of P-site tRNA elbow position (R_{elbow}) and the fraction of uL1m-tRNA contacts ($Q_{L1\text{-}tRNA}$) relative to those formed in the E/E state, calculated from simulations that used the baseline model (left). When uL1m-P-tRNA contacts are attenuated (ΔuL1m model; right), $Q_{L1\text{-}tRNA}$ remains low, consistent with a lack of uL1m binding. **c,** In simulations of P/E formation, perturbations to uL1m and/or mL64 (models ΔuL1m, ΔmL64, and ΔmL64-ΔuL1m models) lead to a wider range of tRNA elbow positions and longer timescales for P/E formation. The narrower range of pathways accessed with the complete/baseline model leads to a lower average value of R_{elbow} as a function of the tRNA CCA position R_{CCA},showing how the corridor favors a process where the elbow motion precedes CCA movement. **d,** Probability distribution (327 simulated events) as a function of elbow and 3′-CCA position reveals distinct intermediates during P/E formation. Representative structural snapshots of I1-I3 are shown in panels e-g. **e**, Intermediate I1 is associated with a small displacement of the tRNA elbow and CCA tail toward the E site. **f,** In order to reach I2, the tRNA elbow is displaced by an additional ~10Å, where it it confined by contacts with mL64. **g,** mL64 then guides the tRNA elbow towards the E site, allowing it to adopt I3. After reaching I3, a final ~40Å displacement of the CCA tail results in adoption of the P/E conformation.

Mitoribosome function is independent of mS29 GTPase activity, but GDP stabilizes intersubunit communication

For each translation step, the movement of mRNA:tRNA is also accompanied by the SSU head swiveling, but it has remained an open question whether intrinsic GTPase activity of mS29 (also known as death-associated protein 3, DAP3) is coupled to the process [63, 64]. We now resolve it by analyzing the structure in two different conformations combined with structure-based mutagenesis and biochemical analysis (Fig. 10, Supplementary Fig. 11a-c). Particularly, we performed site-directed mutagenesis targeting the previously reported nucleotide-binding site [2, 63]

426 and found that the mutant K134A, which based on the structure would affect the nucleotide
427 binding, appears to be dispensable for mitoribosomal function (Supplementary Fig. 11a,b).
428 Recently, another putative binding site has been proposed, formed with residues 173, 177, 208,
429 209, 210, 238, 242, 245, 291, 292, 295 [45, 46] (Fig. 10a,b, Supplementary Fig. 11d), and our map at
430 the local resolution of 2.65 Å suggests the presence of GDP in that site. To address the functional
431 relevance of the GDP, we compared it with the SSU structure in the presence of a
432 nonhydrolyzable analog GMPPNP [45] (Fig. 10a,b). It showed a very similar global architecture of
433 mS29, implying that no net conformational change is involved upon GTP hydrolysis (Fig.
434 10a,b). Furthermore, there is no loss of interactions of mS29 with its binding partners in the SSU
435 head (Fig. 10b). Together, the data suggest that the GTPase activity is not coupled to the
436 translation cycle and the related SSU head swiveling.
437 We next used structural and biochemical analysis to identify the role of the GDP. We compared
438 the interactions of mS29, which is the signature protein of the SSU head with the CP between
439 our classical (2.6 Å resolution) and hybrid (3.0 Å resolution) structures. In the classical state,
440 they are extensive and manifest through three contact sites. Site-1 and -2 are formed between
441 GDP-associated region and the respective mL46 helices α2 and α3 extending from the CP.
442 Contact site-3 is formed with mL48 β-turn protruding into the intersubunit space. Upon subunit
443 ratcheting, in the hybrid state mS29 shifts resulting in disruption of contact site-3. Further, the
444 mS29 β-hairpin 208-216 (stabilized by GDP) that formed contact site-2 in the classical state
445 switches in the hybrid state and remains the only inter-subunit bridge in the dimeter of 50 Å (Fig.
446 10c, Supplementary Fig. 11e). To assess the role of GDP binding in translation, we generated
447 cell lines stably expressing mS29 mutants to disrupt the GDP binding site (Fig. 10d-g,
448 Supplementary Fig. 11a-c).
449 Expression of the double mutants R177A/K245A or R177A/K295A, which target residues
450 interacting with the phosphate groups of GDP, led to reduced levels of mitochondrion-encoded
451 proteins and cellular respiration (Fig. 10d-g, Supplementary Fig. 11c), suggesting a stabilizing
452 role for GDP in this pocket. The R177A/K245A mutation shows only a tendency toward a more
453 stringent effect on mitochondrial protein synthesis than the R177A/K295A mutation in our short
454 15 min pulses. However, the effect is significant when looking at the steady-state levels of
455 mtDNA-encoded proteins. (Fig. 10d,e). Interestingly, the double mutant R177A/H291A
456 displayed a rate of mitochondrial protein synthesis comparable to WT (Fig. 10d-g). Although
457 K245 and K295 stabilize the same beta phosphate on GDP, it is possible that H291 can
458 compensate for the loss of K295, explaining the decreased stability of the R177A/K245A mutant
459 compared to the R177A/K295A mutant. Change of nearby hydrophobic residues Y173A/Y208A
460 yields a decrease in translation similar to the R177A/K245A implying their role in GDP
461 stabilization (Fig. 10d-g). Lastly, double mutant pairs V209P/D238A and Y208A/D238A, which
462 directly disrupt GDP base binding to the mS29 β-hairpin, showed drastic decreases in the
463 synthesis and stability of mitochondrion-encoded proteins (Fig. 10d-g). Thus, the biochemical
464 assays based on mutagenesis show that GDP binding to mS29 is required for efficient
465 mitochondrial translation. Our structure-function correlation analyses suggest that GDP acts as a

stabilizing agent for mS29 β-hairpin 208-216 to maintain the intersubunit communication as tRNA moves to the hybrid state.

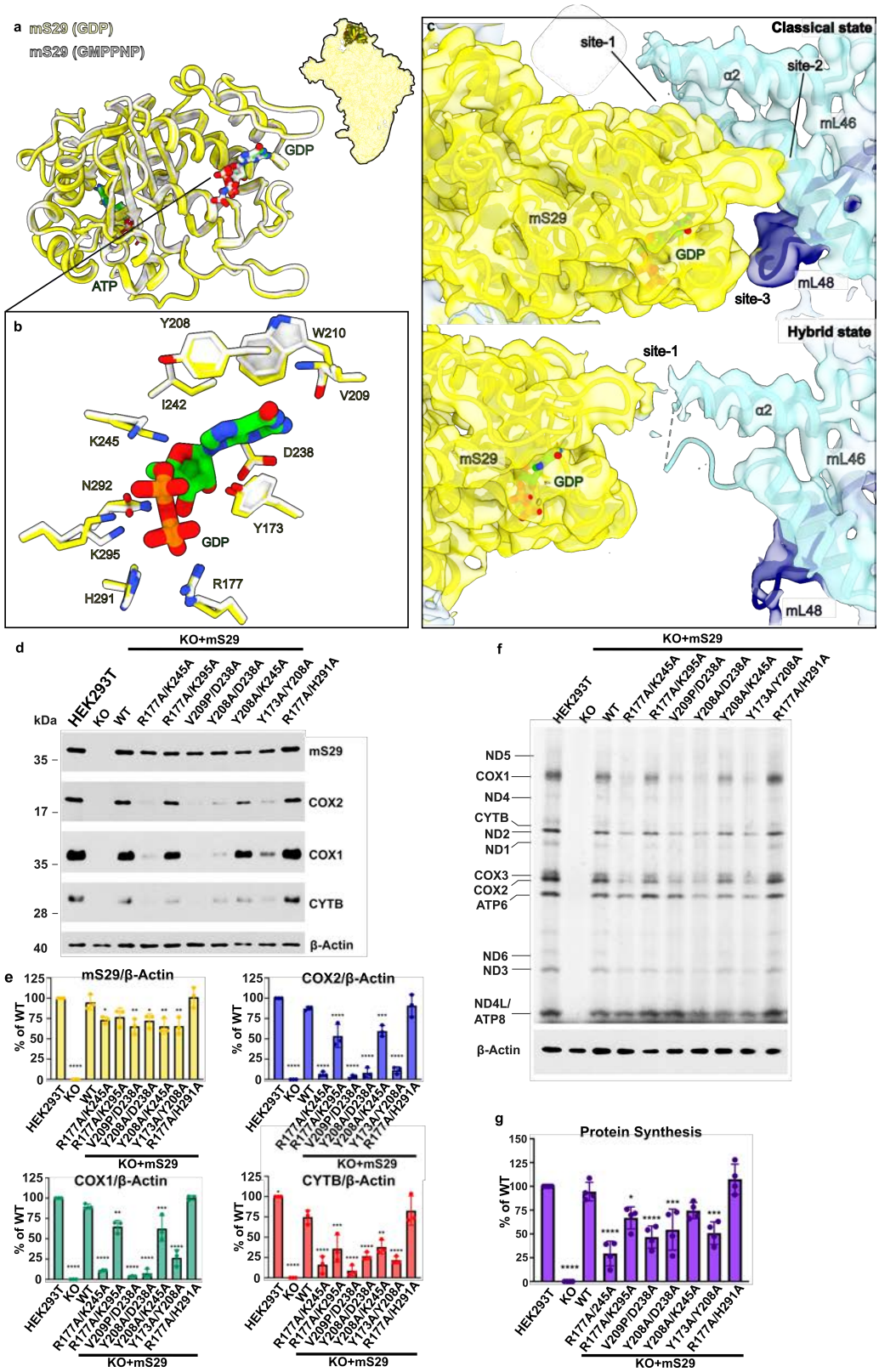

Fig. 10: Binding of GDP to mS29 and role in mitoribosome function.

470 **a,** Superposition of GDP-bound (yellow) and GMPPNP-bound (white) states. **b,** Close-up view
471 illustrating side chains that coordinate nucleotide binding. **c,** Intersubunit contacts in the classical
472 and hybrid states mediated by mS29 (cryo-EM density map shown as colored surface). **d**,
473 Immunoblot analysis comparing steady-state levels of proteins using whole cell lysates from
474 HEK293T (WT), *mS29*-KO (KO), and *mS29*-KO cells stably expressing either WT mS29 or
475 double mutants targeting the GDP-mS29β-hairpin binding site under the control of an attenuated
476 CMV6 promoter (Δ5pCMV6). COX1, COX2, and CTYB were used as markers of mitoribosome
477 function, and β-Actin was used as a loading control. **e**, Images in panel (d) were digitalized, and
478 densitometry was conducted using the histogram function in Adobe Photoshop. The bar graphs
479 represent the mean ± SD from three independent repetitions. Statistical differences were
480 estimated using one-way ANOVA in GraphPad Prism. *p<0.05, **p<0.01; ***p<0.001,
481 ****p<0.0001. **f**, Metabolic labeling of mitochondrially translated peptides in whole cells from
482 the indicated cell lines using ^{35}S-methionine for 15 minutes in the presence of emetine to inhibit
483 cytosolic protein synthesis. Immunoblotting for β-ACTIN was used as a loading control. Newly
484 synthesized peptides are identified on the left. **g**, Images in panel (d) were digitalized, and
485 densitometry was conducted using the histogram function in Adobe Photoshop. The bar graphs
486 represent the mean ± SD from four independent repetitions. Statistical differences were
487 estimated using one-way ANOVA in GraphPad Prism. *p<0.05, **p<0.01; ***p<0.001,
488 ****p<0.0001. The source data file contains all original uncropped and unprocessed
489 immunoblots as well as densitometry values used to perform statistics and generate
490 quantification graphs in panels (d-g).
491

492 **Discussion**

493 This study illustrates the modifications and cofactors of the human mitoribosome (Fig. 1-4,
494 Supplementary Fig. 3-5) and explains how mRNA and tRNAs are stabilized (Fig. 5-9,
495 Supplementary movie 1). While the basic mechanism of translation and the rRNA in the
496 decoding center are conserved, our structures attribute additional roles to mitoribosomal proteins
497 in mRNA and tRNA binding.

498 For mRNA, previous work showed that the delivery of some mitochondrial transcripts for
499 translation is facilitated by the factor LRPPRC [65, 66]. We now demonstrate that once an mRNA is
500 received by the mitoribosome, it involves six mitochondria-specific proteins that sequentially
501 help to direct the mRNA to the decoding center, where it's aligned with a tRNA (Fig. 5,6,
502 Supplementary Fig. 6,8-9). Most of these proteins compensate for the reduced rRNA through the
503 mechanisms of structural patching [67] and protein ratcheting [68] that drive neutral evolution of
504 protein complexity. The first protein to receive an mRNA is mS39, and we detected a co-
505 evolution of mS39 with an mRNA motif Y-N-C-Y that is enriched in all 12 transcripts encoded
506 in the heavy strand of the mitochondrial DNA. The only mRNA that is not enriched with the
507 motif is ND6 (Fig. 5, Supplementary Fig. 7). Interestingly, *ND6* possesses a long 3′UTR and is
508 the only transcript in human mitochondria lacking a polyA tail. This gene is also the only one in
509 mitochondria of vertebrates that was found to be translocated to the control region through gene

510 duplication [69]. This occurs in Antarctic fish species, and while the selectively advantageous
511 duplicate is functionally neutral on the protein level [70], we found that there is a change in the Y-
512 N-C-Y frequency in the mRNA sequence, which is increased by 2-fold (from 14 to 30
513 occurrences in 525 residues). It suggests a possible adaptive correlation between the mRNA
514 stability on the mitoribosome and mt-DNA reorganization.

515 For tRNA, the structure demonstrates two cases with an involvement of mitoribosomal proteins.
516 First, between the A- and P-site tRNAs, the N-terminus of mL40 extends from the CP to the
517 phosphate backbone of mRNA. Second, the recognition of a tRNA in the E-site is achieved by a
518 protein-made L1 stalk region and mL64. Both architectures are unique to mitochondria. Our
519 molecular dynamics simulations further illustrate how the process of E-tRNA movement
520 fundamentally relies on specific protein extensions and insertions of uL1m and uL9m without
521 any involvement of rRNA (Fig. 8,9, Supplementary movie 2). These adaptations of
522 mitoribosomal proteins are particularly important in the context of different functional states, as
523 previous structural studies of elongation [8], termination [10], and rescue [6] complexes reported
524 unidentified densities associated with translational factors, which we now assign specific
525 proteins. Since our data resolves those densities as mammalian protein extensions (Fig. 5,
526 Supplementary Fig. 6), the structural information can now be used for reinterpretation of the
527 functional complexes, thus completing previous works.

528 In addition to proteins, newly revealed structural details include polyamines as stabilizing
529 intramolecular agents in human mitochondria. The visualization of polyamines in the human
530 mitoribosome and the reduced occupancy in the presence of antibiotics further supports their
531 stimulating effect on mitochondrial translation, which is essential for cell proliferation. In
532 mitoribosomes from cell culture treated with antibiotics [45, 71], the occupancy of the polyamines is
533 reduced [45], and they are generally replaced with Mg^{2+}or K^{+}, accompanied by some residue
534 rearrangement (Supplementary Fig. 5). Those changes are associated with attenuation of
535 translation, and thus our structure rationalizes previous report that the positive effect of
536 polyamines could not be functionally replaced by the addition of Mg^{2+} in a cell-free system [72].
537 Together, it links mitochondrial translation to reports assigning key regulatory effects to
538 polyamines in mitochondria. This includes anti-inflammatory effects and inhibition of aging-
539 associated pathologies upon consumption of polyamine in mice [31, 32, 73], the ability to boost
540 mitochondrial respiratory capacity in a *Drosophila* aging model [32], restorative effects on
541 oxidative functions of aged mitochondria [74, 75], and antitumor immunity in aged mice [76].
542 Polyamines were also proposed to regulate mitochondrial metabolism via Src kinase signaling to
543 preserve bioenergetics in the spinal cord [77]. Considering our results on the involvement of iron-
544 sulphur clusters as protein-protein mediating agents [45], as well as in the mitoribosomal assembly
545 [78], the new structural data provides a wealth of additional information on cofactors that can be
546 further assessed in disease models and with respect to tissue and cell specificity, as well as
547 ageing processes. The detection of disulfide bond in mS37 that was proposed to occur during the
548 mitochondrial protein import pathway [47] further links translation with metabolic state and

549 NADH/NAD$^+$ ratio in the intermembrane space and the matrix due to the special role of mS37
550 that links assembly to the initiation of translation [25].
551 On the rRNA level, through tailored quantitative mass-spectrometry, we describe a fully
552 modified mitoribosome, including in the decoding center. While the critical modifications are
553 conserved with bacteria, an unexpected feature of the structure is that the rRNA component CP-
554 tRNA^{Val} is modified, as well as aminoacylated. This suggests that this tRNA is recognized in the
555 matrix by the elongation factor mtEF-Tu prior the assembly onto the CP. The involvement
556 mtEF-Tu in the mitoribosome assembly has been previously reported, and direct interaction with
557 the assembly factor GTPBP5 was visualized by cryo-EM of an LSU intermediate [79]. Thus, the
558 regulation of the assembly of the mammalian mitoribosome relies on the availability of mtEF-Tu
559 in active developmental stages of the organelle, which might be a potential early checkpoint for
560 translation. A possible model for these observations is that accumulation of deacylated tRNAs
561 might trigger starvation responses, and since tRNA^{Val} is likely to be abundant at the onset of
562 mitoribosomal assembly, its aminoacylation is essential, which requires the presence of mtEF-
563 Tu. The feature is likely to be mammalian-specific, as representative from other lineages, such as
564 fungi [46], ciliates [80], and algae [81, 82] do not possess the CP-tRNA component in their
565 mitoribosomes.

566 Finally, the data addresses a long-standing question of whether a putative GTPase and death-
567 associated protein mS29 might provide the human mitoribosome with an intrinsic activity, while
568 undergoing structural rearrangements. This protein is of a particular clinical interest, because
569 several cancer types are associated with its aberrant expression [83]. We show that mS29-GDP
570 does not change its conformation during translation but is a stable structural element that
571 contributes to inter-subunit communication during transitions between classical and hybrid states
572 (Fig. 10, Supplementary Fig. 11).

573 Overall, these data explain how the newly identified components modulate the functional and
574 structurally distinct mitoribosome. With the continuous progress in improvement of resolution of
575 cryo-EM reconstructions, and availability of newly developed methods for base editing of
576 protein-coding genes in mammalian mitochondrial genome [84, 85], the field of mitochondrial
577 translation now steps into a phase, where it becomes possible to analyze fine regulatory
578 mechanisms specific transcripts, and study how it's affected by modifications, cofactors, and
579 mutants. Therefore, the structural approach has a potential to lead towards a more detailed
580 description of the mitoribosome-associated pathologies, including mitochondrial disease and
581 ageing, and the current study will provide a reference model of the human mitoribosome for
582 future investigation.

583

584 **References**

585 1. Kienzle L*, et al.* A small protein coded within the mitochondrial canonical gene nd4
586 regulates mitochondrial bioenergetics. *BMC Biol* **21**, 111 (2023).
587

588 2. Amunts A, Brown A, Toots J, Scheres SHW, Ramakrishnan V. Ribosome. The structure
589 of the human mitochondrial ribosome. *Science* **348**, 95-98 (2015).
590
591 3. Ferrari A, Del'Olio S, Barrientos A. The Diseased Mitoribosome. *FEBS Lett* **595**, 1025-
592 1061 (2021).
593
594 4. Amarasekera SSC*, et al.* Multi-omics identifies large mitoribosomal subunit instability
595 caused by pathogenic MRPL39 variants as a cause of pediatric onset mitochondrial
596 disease. *Hum Mol Genet*, (2023).
597
598 5. Aibara S, Singh V, Modelska A, Amunts A. Structural basis of mitochondrial translation.
599 *Elife* **9**, (2020).
600
601 6. Desai N, Yang H, Chandrasekaran V, Kazi R, Minczuk M, Ramakrishnan V.
602 Elongational stalling activates mitoribosome-associated quality control. *Science* **370**,
603 1105-1110 (2020).
604
605 7. Koripella RK*, et al.* Structures of the human mitochondrial ribosome bound to EF-G1
606 reveal distinct features of mitochondrial translation elongation. *Nat Commun* **11**, 3830
607 (2020).
608
609 8. Kummer E, Ban N. Structural insights into mammalian mitochondrial translation
610 elongation catalyzed by mtEFG1. *EMBO J* **39**, e104820 (2020).
611
612 9. Kummer E*, et al.* Unique features of mammalian mitochondrial translation initiation
613 revealed by cryo-EM. *Nature* **560**, 263-267 (2018).
614
615 10. Kummer E, Schubert KN, Schoenhut T, Scaiola A, Ban N. Structural basis of translation
616 termination, rescue, and recycling in mammalian mitochondria. *Mol Cell* **81**, 2566-2582
617 e2566 (2021).
618
619 11. Rebelo-Guiomar P, Powell CA, Van Haute L, Minczuk M. The mammalian
620 mitochondrial epitranscriptome. *Biochim Biophys Acta Gene Regul Mech* **1862**, 429-446
621 (2019).
622
623 12. D'Souza AR, Minczuk M. Mitochondrial transcription and translation: overview. *Essays*
624 *Biochem* **62**, 309-320 (2018).
625
626 13. Garone C*, et al.* Defective mitochondrial rRNA methyltransferase MRM2 causes
627 MELAS-like clinical syndrome. *Hum Mol Genet* **26**, 4257-4266 (2017).
628
629 14. Lopez Sanchez MIG, Cipullo M, Gopalakrishna S, Khawaja A, Rorbach J. Methylation
630 of Ribosomal RNA: A Mitochondrial Perspective. *Front Genet* **11**, 761 (2020).
631

632 15. Antonicka H, Choquet K, Lin ZY, Gingras AC, Kleinman CL, Shoubridge EA. A
633 pseudouridine synthase module is essential for mitochondrial protein synthesis and cell
634 viability. *EMBO Rep* **18**, 28-38 (2017).
635
636 16. Baer RJ, Dubin DT. Methylated regions of hamster mitochondrial ribosomal RNA:
637 structural and functional correlates. *Nucleic Acids Res* **9**, 323-337 (1981).
638
639 17. McCulloch V, Seidel-Rogol BL, Shadel GS. A human mitochondrial transcription factor
640 is related to RNA adenine methyltransferases and binds S-adenosylmethionine. *Mol Cell*
641 *Biol* **22**, 1116-1125 (2002).
642
643 18. Metodiev MD*, et al.* Methylation of 12S rRNA is necessary for in vivo stability of the
644 small subunit of the mammalian mitochondrial ribosome. *Cell Metab* **9**, 386-397 (2009).
645
646 19. Metodiev MD*, et al.* NSUN4 is a dual function mitochondrial protein required for both
647 methylation of 12S rRNA and coordination of mitoribosomal assembly. *PLoS Genet* **10**,
648 e1004110 (2014).
649
650 20. Seidel-Rogol BL, McCulloch V, Shadel GS. Human mitochondrial transcription factor
651 B1 methylates ribosomal RNA at a conserved stem-loop. *Nat Genet* **33**, 23-24 (2003).
652
653 21. Sergiev PV, Aleksashin NA, Chugunova AA, Polikanov YS, Dontsova OA. Structural
654 and evolutionary insights into ribosomal RNA methylation. *Nat Chem Biol* **14**, 226-235
655 (2018).
656
657 22. Van Haute L*, et al.* METTL15 introduces N4-methylcytidine into human mitochondrial
658 12S rRNA and is required for mitoribosome biogenesis. *Nucleic Acids Res* **47**, 10267-
659 10281 (2019).
660
661 23. Zaganelli S*, et al.* The Pseudouridine Synthase RPUSD4 Is an Essential Component of
662 Mitochondrial RNA Granules. *J Biol Chem* **292**, 4519-4532 (2017).
663
664 24. Hillen HS*, et al.* Structural basis of GTPase-mediated mitochondrial ribosome biogenesis
665 and recycling. *Nat Commun* **12**, 3672 (2021).
666
667 25. Itoh Y*, et al.* Mechanism of mitoribosomal small subunit biogenesis and preinitiation.
668 *Nature* **606**, 603-608 (2022).
669
670 26. Harper NJ, Burnside C, Klinge S. Principles of mitoribosomal small subunit assembly in
671 eukaryotes. *Nature* **614**, 175-181 (2023).
672
673 27. Bobba-Alves N*, et al.*, (2022).
674
675 28. Haas RH. Mitochondrial Dysfunction in Aging and Diseases of Aging. *Biology (Basel)* **8**,
676 (2019).
677

678 29. Hong HJ, *et al.* Mitoribosome insufficiency in beta cells is associated with type 2
679 diabetes-like islet failure. *Exp Mol Med* **54**, 932-945 (2022).
680
681 30. Richman TR, *et al.* Mitochondrial mistranslation modulated by metabolic stress causes
682 cardiovascular disease and reduced lifespan. *Aging Cell* **20**, e13408 (2021).
683
684 31. Soda K, Dobashi Y, Kano Y, Tsujinaka S, Konishi F. Polyamine-rich food decreases age-
685 associated pathology and mortality in aged mice. *Exp Gerontol* **44**, 727-732 (2009).
686
687 32. Soda K, Kano Y, Chiba F, Koizumi K, Miyaki Y. Increased polyamine intake inhibits
688 age-associated alteration in global DNA methylation and 1,2-dimethylhydrazine-induced
689 tumorigenesis. *PLoS One* **8**, e64357 (2013).
690
691 33. Medina CB, *et al.* Metabolites released from apoptotic cells act as tissue messengers.
692 *Nature* **580**, 130-135 (2020).
693
694 34. Igarashi K, Kashiwagi K. The functional role of polyamines in eukaryotic cells. *Int J*
695 *Biochem Cell Biol* **107**, 104-115 (2019).
696
697 35. Mandal S, Mandal A, Johansson HE, Orjalo AV, Park MH. Depletion of cellular
698 polyamines, spermidine and spermine, causes a total arrest in translation and growth in
699 mammalian cells. *Proc Natl Acad Sci U S A* **110**, 2169-2174 (2013).
700
701 36. Zivanov J, *et al.* New tools for automated high-resolution cryo-EM structure
702 determination in RELION-3. *Elife* **7**, (2018).
703
704 37. Zivanov J, Nakane T, Scheres SHW. A Bayesian approach to beam-induced motion
705 correction in cryo-EM single-particle analysis. *IUCrJ* **6**, 5-17 (2019).
706
707 38. Zivanov J, Nakane T, Scheres SHW. Estimation of high-order aberrations and anisotropic
708 magnification from cryo-EM data sets in RELION-3.1. *IUCrJ* **7**, 253-267 (2020).
709
710 39. Scheres SH. Processing of Structurally Heterogeneous Cryo-EM Data in RELION.
711 *Methods Enzymol* **579**, 125-157 (2016).
712
713 40. Taoka M, *et al.* A mass spectrometry-based method for comprehensive quantitative
714 determination of post-transcriptional RNA modifications: the complete chemical
715 structure of Schizosaccharomyces pombe ribosomal RNAs. *Nucleic Acids Res* **43**, e115
716 (2015).
717
718 41. Brown A, *et al.* Structure of the large ribosomal subunit from human mitochondria.
719 *Science* **346**, 718-722 (2014).
720
721 42. Brown A, *et al.* Structures of the human mitochondrial ribosome in native states of
722 assembly. *Nat Struct Mol Biol* **24**, 866-869 (2017).
723

43. Greber BJ, *et al.* The complete structure of the large subunit of the mammalian mitochondrial ribosome. *Nature* **515**, 283-286 (2014).

44. Suzuki T, *et al.* Complete chemical structures of human mitochondrial tRNAs. *Nat Commun* **11**, 4269 (2020).

45. Itoh Y, *et al.* Structure of the mitoribosomal small subunit with streptomycin reveals Fe-S clusters and physiological molecules. *Elife* **11**, (2022).

46. Itoh Y, Naschberger A, Mortezaei N, Herrmann JM, Amunts A. Analysis of translating mitoribosome reveals functional characteristics of translation in mitochondria of fungi. *Nat Commun* **11**, 5187 (2020).

47. Peker E, *et al.* A two-step mitochondrial import pathway couples the disulfide relay with matrix complex I biogenesis. *J Cell Biol* **222**, (2023).

48. Watson ZL, *et al.* Structure of the bacterial ribosome at 2 A resolution. *Elife* **9**, (2020).

49. Jourdain AA, *et al.* A mitochondria-specific isoform of FASTK is present in mitochondrial RNA granules and regulates gene expression and function. *Cell Rep* **10**, 1110-1121 (2015).

50. Takyar S, Hickerson RP, Noller HF. mRNA helicase activity of the ribosome. *Cell* **120**, 49-58 (2005).

51. Khawaja A, *et al.* Distinct pre-initiation steps in human mitochondrial translation. *Nat Commun* **11**, 2932 (2020).

52. Selmer M, *et al.* Structure of the 70S ribosome complexed with mRNA and tRNA. *Science* **313**, 1935-1942 (2006).

53. Rozov A, *et al.* Importance of potassium ions for ribosome structure and function revealed by long-wavelength X-ray diffraction. *Nat Commun* **10**, 2519 (2019).

54. Bhaskar V, *et al.* Dynamics of uS19 C-Terminal Tail during the Translation Elongation Cycle in Human Ribosomes. *Cell Rep* **31**, 107473 (2020).

55. Ogle JM, Brodersen DE, Clemons WM, Jr., Tarry MJ, Carter AP, Ramakrishnan V. Recognition of cognate transfer RNA by the 30S ribosomal subunit. *Science* **292**, 897-902 (2001).

56. Youngman EM, Cochella L, Brunelle JL, He S, Green R. Two distinct conformations of the conserved RNA-rich decoding center of the small ribosomal subunit are recognized by tRNAs and release factors. *Cold Spring Harb Symp Quant Biol* **71**, 545-549 (2006).

57. Nakayama H, *et al.* Ariadne: a database search engine for identification and chemical analysis of RNA using tandem mass spectrometry data. *Nucleic Acids Res* **37**, e47 (2009).

58. Yamauchi Y, *et al.* A mass spectrometry-based method for direct determination of pseudouridine in RNA. *Nucleic Acids Res* **44**, e59 (2016).

59. Nishimura K, *et al.* Identification of the RsmG methyltransferase target as 16S rRNA nucleotide G527 and characterization of Bacillus subtilis rsmG mutants. *J Bacteriol* **189**, 6068-6073 (2007).

60. Noel JK, *et al.* SMOG 2: A Versatile Software Package for Generating Structure-Based Models. *PLoS Comput Biol* **12**, e1004794 (2016).

61. Whitford PC, Noel JK, Gosavi S, Schug A, Sanbonmatsu KY, Onuchic JN. An all-atom structure-based potential for proteins: bridging minimal models with all-atom empirical forcefields. *Proteins* **75**, 430-441 (2009).

62. Polikanov YS, Melnikov SV, Soll D, Steitz TA. Structural insights into the role of rRNA modifications in protein synthesis and ribosome assembly. *Nat Struct Mol Biol* **22**, 342-344 (2015).

63. Greber BJ, *et al.* Ribosome. The complete structure of the 55S mammalian mitochondrial ribosome. *Science* **348**, 303-308 (2015).

64. Ott M, Amunts A, Brown A. Organization and Regulation of Mitochondrial Protein Synthesis. *Annu Rev Biochem* **85**, 77-101 (2016).

65. Singh V, *et al.* Structural basis of LRPPRC-SLIRP-dependent translation by the mitoribosome. *bioRxiv*, 2022.2006.2020.496763 (2022).

66. Webster MW, *et al.* Structural basis of transcription-translation coupling and collision in bacteria. *Science* **369**, 1355-1359 (2020).

67. Petrov AS, Wood EC, Bernier CR, Norris AM, Brown A, Amunts A. Structural Patching Fosters Divergence of Mitochondrial Ribosomes. *Mol Biol Evol* **36**, 207-219 (2019).

68. Hochberg GKA, Liu Y, Marklund EG, Metzger BPH, Laganowsky A, Thornton JW. A hydrophobic ratchet entrenches molecular complexes. *Nature* **588**, 503-508 (2020).

69. Zhuang X, Cheng CH. ND6 gene "lost" and found: evolution of mitochondrial gene rearrangement in Antarctic notothenioids. *Mol Biol Evol* **27**, 1391-1403 (2010).

70. Mark FC, *et al.* Mitochondrial function in Antarctic nototheniids with ND6 translocation. *PLoS One* **7**, e31860 (2012).

71. Itoh Y, *et al.* Mechanism of membrane-tethered mitochondrial protein synthesis. *Science* **371**, 846-849 (2021).

72. Ogasawara T, Ito K, Igarashi K. Effect of polyamines on globin synthesis in a rabbit reticulocyte polyamine-free protein synthetic system. *J Biochem* **105**, 164-167 (1989).

73. Schroeder S, *et al.* Dietary spermidine improves cognitive function. *Cell Rep* **35**, 108985 (2021).

74. Jing YH, *et al.* Spermidine ameliorates the neuronal aging by improving the mitochondrial function in vitro. *Exp Gerontol* **108**, 77-86 (2018).

75. Phillips JE, Chaffee RR. Restorative effects of spermine on oxidative phosphorylation and respiration in heat-aged mitochondria. *Biochem Biophys Res Commun* **108**, 174-181 (1982).

76. Al-Habsi M, *et al.* Spermidine activates mitochondrial trifunctional protein and improves antitumor immunity in mice. *Science* **378**, eabj3510 (2022).

77. Zhang R, Ma XN, Liu K, Zhang L, Yao M. Exogenous spermine preserves mitochondrial bioenergetics via regulating Src kinase signaling in the spinal cord. *Mol Med Rep* **16**, 3619-3626 (2017).

78. Ast T, *et al.* METTL17 is an Fe-S cluster checkpoint for mitochondrial translation. *bioRxiv*, 2022.2011.2024.517765 (2022).

79. Cipullo M, Gese GV, Khawaja A, Hallberg BM, Rorbach J. Structural basis for late maturation steps of the human mitoribosomal large subunit. *Nat Commun* **12**, 3673 (2021).

80. Tobiasson V, Amunts A. Ciliate mitoribosome illuminates evolutionary steps of mitochondrial translation. *Elife* **9**, (2020).

81. Tobiasson V, Gahura O, Aibara S, Baradaran R, Zikova A, Amunts A. Interconnected assembly factors regulate the biogenesis of mitoribosomal large subunit. *EMBO J* **40**, e106292 (2021).

82. Waltz F, Soufari H, Bochler A, Giege P, Hashem Y. Cryo-EM structure of the RNA-rich plant mitochondrial ribosome. *Nat Plants* **6**, 377-383 (2020).

83. Sui L, *et al.* Death associated protein-3 (DAP3) and DAP3 binding cell death enhancer-1 (DELE1) in human colorectal cancer, and their impacts on clinical outcome and chemoresistance. *Int J Oncol* **62**, (2023).

84. Silva-Pinheiro P, *et al.* A library of base editors for the precise ablation of all protein-coding genes in the mouse mitochondrial genome. *Nat Biomed Eng*, (2022).

85. Willis JCW, Silva-Pinheiro P, Widdup L, Minczuk M, Liu DR. Compact zinc finger base editors that edit mitochondrial or nuclear DNA in vitro and in vivo. *Nat Commun* **13**, 7204 (2022).

Methods

Experimental model and culturing

HEK293S-derived cells (T501) were grown in Freestyle 293 Expression Medium containing 5% tetracycline-free fetal bovine serum (FBS) in vented shaking flasks at 37°C, 5% CO_2 and 120 rpm (550 x g). Culture was scaled up sequentially, by inoculating at 1.5 x 10^6 cells/mL and subsequently splitting at a cell density of 3.0 x 10^6 cells/mL. Finally, a final volume of 2 L of cell culture at a cell density of 4.5 x 10^6 cells/mL was used for mitochondria isolation, as previously described [86].

mS29-KO cells were derived from HEK293T (CRL-3216) and cultured in complete DMEM supplemented with 20% FBS at 37 °C and 5% CO_2. HEK293T (CRL-3216) were cultured in high-glucose, sodium pyruvate, L-glutamine Dulbecco's modified Eagle medium (DMEM, Life Technologies) supplemented with 10% FBS, 100 µg/mL uridine, 3 mM sodium formate, and 1x MEM non-essential amino acids complete DMEM medium). Analysis of mycoplasma contamination was routinely performed.

For the labeling of cells with deuterated Uridine required for SILNAS analysis, TK6 cells deficient in uridine monophosphate synthase (*UMPS-/-*) were cultured at 37°C in RPMI-1640 medium containing 10% horse serum, 2 mM L-glutamine, penicillin (50 U/ml), streptomycin (50 µg/ml) and 0.1 mM 5,6-D2-uridine.

Generation of mS29 edited cell lines and plasmid transfections

To generate a stable human *mS29-KO* cell line in HEK293T cells (ATCC: CRL-3216), we used a pool of CRISPR/Cas9-mediated knockout cells generated by the genome editing company, Synthego (Synthego Corporation, Redwood City, CA). HEK293T cells were first tested to be negative for mycoplasma. Three guide RNAs targeting exon 5 of the *mS29* gene (DAP3-202 transcript ID ENST00000368336.10) were selected for high specificity and activity to create premature stop codons through frameshift mutations in the coding region via insertions and/or deletions (Indels). Targeting exon 5 ensured that all *mS29* transcript variants would be affected. Based on additional off-target analysis, the three specific guide RNAs selected (g1, g2, and g3) were: g1 5′-GUGAAGCUUGCCUGAUGGUA-3′ [AGG]-PAM, g2 5′-UAUAGCUGGAUAAGCAAAAC-3′ [TGG]-PAM, and g3 5′-AUGCUUUCUCCCCUCAAAUA-3′ [AGG]-PAM. The pool of knockout cells was then generated by electroporation of ribonucleoproteins (RNPs) containing the Cas9 protein and synthetic chemically modified sgRNA (Synthego) into the cells using Synthego's optimized protocol. The editing efficiency was assessed upon recovery, 48 h post-electroporation. Genomic

899 DNA is extracted from a portion of the cells, PCR-amplified, and sequenced using Sanger
900 sequencing. The resulting chromatograms are processed using Synthego Inference of CRISPR
901 Edits software (ice.synthego.com). The pooled *mS29-KO* was then plated into 96-well plates to
902 screen for single clones in-house. Single clone candidates were screened by immunoblotting to
903 determine the steady-state levels of mS29 and the mtDNA-encoded COX2 protein as a surrogate
904 of mitochondrial protein synthesis capacity. Clones that had undetectable mS29 and attenuated
905 COX2 levels were further analyzed by genotyping. For genotyping, the edited region of mS29
906 was amplified using oligonucleotides mS29 exon 5 seq (-164) Forward: 5′-
907 GGATAGATTTTCAAACTCAGTACCA-3′ and mS29 exon 5 seq (+166) Reverse: 5′-
908 TCCTGACTTCAGGCGATACG-3′, and subsequently cloned into the TOPO-TA vector
909 (Thermo Fisher) for sequencing.

910 To establish a stable cell line reconstituted with mS29, we obtained the WT *mS29* gene as a
911 Myc/DDK-tagged ORF from Origene (Cat# RC223182). Using restriction sites *Asi*SI and *Pme*I,
912 WT mS29-Myc/DDK was cloned into a mammalian vector with hygromycin as the selection
913 marker. The vector used was pCMV6, in which mS29 gene expression was placed under the
914 control of an attenuated version of the human cytomegalovirus (CMV) enhancer/promoter (Δ5)
915 in which a deletion in the promoter sequence eliminates most transcription factor binding sites [87].
916 Furthermore, to ensure functionality of the recombinant mS29, the Myc/DDK tag was removed
917 via the Q5 site-directed mutagenesis kit (New England Biolabs) using the oligonucleotides mS29
918 ΔMyc-DDK Forward: 5′-TAAACGGCCGGCCGCGGT-3′ and mS29 Δmyc-DDK Reverse: 5′-
919 GAGGTAGGCACAGTGCCGCTC-3′. Two µg of the construct containing *mS29* was
920 transfected to the HEK293T *mS29*-KO cell line using 5 µL of EndoFectin™ Max (GeneCopoeia)
921 pre-incubated in Opti-MEM (ThermoFisher). 72 h post-transfection, the medium was
922 supplemented with 200µg/mL hygromycin B for three weeks. We use the same protocol to
923 establish stable cell lines reconstituted with mutant variants of mS29.

924 Mutant variants of the *mS29*-containing construct were generated using the Q5 site-directed
925 mutagenesis kit (New England Biolabs). Mutagenesis primers were designed using the
926 NEBaseChanger tool. Oligonucleotides used for mutagenesis include: mS29 K134A Forward:
927 5′-GGGAACAGGAGCAACCCTAAGTC-3′; mS29 K134A Reverse: 5′-
928 TTCTCTCCATACAGAAGATATC-3′; mS29 Y173A Forward: 5′-
929 GCAGTCCAGCGCCAACAAACAGC-3′; mS29 Y173A Reverse: 5′-
930 AGAAGATCCCGACAATTTTTC-3′; mS29 R177A Forward: 5′-
931 CAACAAACAGGCCTTTGATCAACCTTTAGAG-3′; mS29 R177A Reverse: 5′-
932 TAGCTGGACTGCAGAAGA-3′; mS29 K245A Forward: 5′-
933 AATTGTGCTGGCAGAGCTAAAGAGGC-3′; mS29 K245A Reverse: 5′-
934 CCAACTGCATCTGTGGCG-3′; mS29 H291A Forward: 5′-
935 AGCACTTGTTGCCAACTTGAGGAAAATGATG-3′; mS29 H291A Reverse: 5′-
936 AATTCCTCGGGGGCAATC-3′; mS29 K295A Forward: 5′-
937 CAACTTGAGGGCAATGATGAAAAATGATTG-3′; mS29 K295A Reverse: 5′-
938 TGAACAAGTGCTAATTCC-3′; mS29 Y208A Forward: 5’-

939 TCAAGAGAAGGCTGTCTGGAATAAGAG -3'; mS29 Y208A Reverse: 5'-
940 ACTTTTATCTGGTTCAGG -3'; mS29 V209P Forward: 5'-
941 AGAGAAGTATCCCTGGAATAAGAGAG -3'; mS29 V209P Reverse: 5'-
942 TGAACTTTTATCTGGTTCAG -3'; mS29 D238A Forward: 5'-
943 GAACGCCACAGCTGCAGTTGGAA -3'; mS29 D238A Reverse: 5'-
944 CTCACCCGTGTTATGCCC -3. All mutant sequences were validated by Sanger sequencing
945 using oligonucleotides Δ5pCMV6 Forward: 5′-CCTCTTCGCTATTACGCCAG-3′, mS29
946 cDNA (308) Forward: 5′-AACCAGCCCTAGAACTTCTGC-3′, and mS29 cDNA (829)
947 Forward: 5′-GAAGATAAAAGCCCGATTGC-3′.
948

949 Mitoribosome purification

950 Mitoribosome purification was carried out based on the previously developed protocol for rapid
951 isolation [86]. HEK293S-derived cells were harvested from the 2 L culture when the cell density
952 was 4.2 x 10^6 cells/mL by centrifugation at 1,000 g for 7 min, 4 °C. The pellet was washed and
953 resuspended in 200 mL Phosphate Buffered Saline (PBS). The washed cells were pelleted at
954 1,000 g for 10 min at 4 °C. The resulting pellet was resuspended in 120 mL of MIB buffer (50
955 mM HEPES-KOH, pH 7.5, 10 mM KCl, 1.5 mM $MgCl_2$, 1 mM EDTA, 1 mM EGTA, 1 mM
956 dithiothreitol, cOmplete EDTA-free protease inhibitor cocktail (Roche) and allowed to swell in
957 the buffer for 15 min in the cold room by gentle stirring. About 45 mL of SM4 buffer (840 mM
958 mannitol, 280 mM sucrose, 50 mM HEPES-KOH, pH 7.5, 10 mM KCl, 1.5 mM $MgCl_2$, 1 mM
959 EDTA, 1 mM EGTA, 1 mM DTT, 1X cOmplete EDTA-free protease inhibitor cocktail (Roche)
960 was added to the cells in being stirred in MIB buffer and poured into a nitrogen cavitation device
961 kept on ice. The cells were subjected to a pressure of 500 psi for 20 min before releasing the
962 nitrogen from the chamber and collecting the lysate. The lysate was clarified by centrifugation at
963 800 x g and 4 °C, for 15 min, to separate the cell debris and nuclei. The supernatant was passed
964 through a cheesecloth into a beaker kept on ice. The pellet was resuspended in half the previous
965 volume of MIBSM buffer (3 volumes MIB buffer + 1 volume SM4 buffer) and homogenized
966 with a Teflon/glass Dounce homogenizer. After clarification as described before, the resulting
967 lysate was pooled with the previous batch of the lysate and subjected to centrifugation at 1,000 x
968 g, 4 °C for 15 minutes to ensure complete removal of cell debris. The clarified and filtered
969 supernatant was centrifuged at 10,000 x g and 4 °C for 15 min to pellet crude mitochondria.
970 Crude mitochondria were resuspended in 10 mL MIBSM buffer and treated with 200 units of
971 Rnase-free Dnase (Sigma-Aldrich) for 20 min in the cold room to remove contaminating
972 genomic DNA. Crude mitochondria were again recovered by centrifugation at 10,000 g, 4 °C for
973 15 min and gently resuspended in 2 mL SEM buffer (250 mM sucrose, 20 mM HEPES-KOH,
974 pH 7.5, 1 mM EDTA). Resuspended mitochondria were subjected to a sucrose density step-
975 gradient (1.5 mL of 60% sucrose; 4 mL of 32% sucrose; 1.5 mL of 23% sucrose and 1.5 mL of
976 15% sucrose in 20 mM HEPES-KOH, pH 7.5, 1 mM EDTA) centrifugation in a Beckmann
977 Coulter SW40 rotor at 28,000 rpm (139,000 x g) for 60 min. Mitochondria seen as a brown band

978 at the interface of 32% and 60% sucrose layers were collected and snap-frozen using liquid
979 nitrogen and transferred to −80 °C.

980 Frozen mitochondria were transferred on ice and allowed to thaw slowly. Lysis buffer (25 mM
981 HEPES-KOH, pH 7.5, 50 mM KCl, 10 mM $Mg(OAc)_2$, 2% polyethylene glycol octylphenyl
982 ether, 2 mM DTT, 1 mg/mL EDTA-free protease inhibitors (Sigma-Aldrich) was added to
983 mitochondria and the tube was inverted several times to ensure mixing. A small Teflon/glass
984 Dounce homogenizer was used to homogenize mitochondria for efficient lysis. After incubation
985 on ice for 5-10 min, the lysate was clarified by centrifugation at 30,000 x g for 20 min, 4 °C. The
986 clarified lysate was carefully collected. Centrifugation was repeated to ensure complete
987 clarification. A volume of 1 mL of the mitochondrial lysate was applied on top of 0.4 mL of 1 M
988 sucrose (v/v ratio of 2.5:1) in thick-walled TLS55 tubes. Centrifugation was carried out at
989 231,500 x g for 45 min in a TLA120.2 rotor at 4 °C. The pellets thus obtained were washed and
990 sequentially resuspended in a total volume of 100 µl resuspension buffer (20 mM HEPES-KOH,
991 pH 7.5, 50 mM KCl, 10 mM $Mg(OAc)_2$, 1% Triton X-100, 2 mM DTT). The sample was
992 clarified twice by centrifugation at 18,000 g for 10 min at 4 °C. The sample was applied on to a
993 linear 15-30% sucrose (20 mM HEPES-KOH, pH 7.5, 50 mM KCl, 10 mM $Mg(OAc)_2$, 0.05% n-
994 dodecyl-β-D-maltopyranoside, 2 mM DTT) gradient and centrifuged in a TLS55 rotor at 213,600
995 x g for 120 min at 4 °C. The gradient was fractionated into 50 µL volume aliquots. The
996 absorption for each aliquot at 260 nm was measured and fractions corresponding to the
997 monosome peak were collected. The pooled fractions were subjected to buffer exchange with the
998 resuspension buffer to dilute away sucrose.

999

1000 <u>rRNA mass spectrometry</u>

1001 *Purification of mitochondrial rRNAs*

1002 Mitochondrial rRNAs of the HEK293 cells were extracted from the purified ribosome using
1003 Isogen (Nippon Gene) and stored at -80 °C until use. TK6 cell culture (~1.0×10^9 cells) were
1004 homogenized by Dounce homogenizer with 250 mM sucrose, 1 mM EDTA and 10 mM
1005 Tris−HCl (pH 8.0). The lysate was centrifuged twice at 1500 x g for 3 min at 4 °C, and the
1006 resulting supernatant was further centrifuged at 5000 x g for 10 min to obtain mitochondrial
1007 precipitate. From the precipitate, total mitochondrial RNA (~100 µg) was extracted using TRIzol
1008 Reagent (Thermo Fisher Scientific).

1009 Each mitochondrial rRNA was purified by using reversed-phase LC through a PLRP-S 4000Å
1010 column (4.6 × 150 mm, 10 µm, Agilent Technologies). After applying the mixture of rRNAs
1011 from the purified ribosome or total mitochondrial RNA to the column, the rRNAs were eluted
1012 with a 60-minute linear gradient of 11.5–13.5% (v/v) acetonitrile in 100 mM TEAA (pH 7.0) and
1013 0.1 mM diammonium phosphate at a flow rate of 200 µl/min at 60 °C while monitoring the
1014 eluate at A260 [88].

1015

1016 *LC-MS, MS/MS and MS/MS/MS analysis and database search of RNA fragments*

1017 RNA was digested as described below. Nucleolytic RNA fragments were analyzed with a direct
1018 nanoflow LC-MS system as described [89]. The LC eluate was sprayed online at –1.3 kV with the
1019 aid of a spray-assisting device [89] to a Q Exactive Plus mass spectrometer (Thermo Fisher
1020 Scientific) in negative ion mode. Other settings for MS, MS/MS and MS/MS/MS were as
1021 described [58].

1022 Ariadne [57] was used for database searches and assignment of MS/MS RNA spectra. The
1023 composite of human cytosolic and mitochondrial rRNA and tRNA sequences was used as a
1024 database. The following default search parameters for Ariadne were used: maximum number of
1025 missed cleavages, 1; variable modification parameters, two methylations per RNA fragment for
1026 any residue; RNA mass tolerance, ±5 ppm, and MS/MS tolerance, ±20 ppm. For assignment of
1027 Ψ residues using 5,6-D2-uridine labeled RNAs, the mass table and the variable modification
1028 parameters were altered from default values to "5,6D_CU" and "Ψ", respectively, because both
1029 C and U were labeled with the medium and the pseudouridylation reaction results in the
1030 exchange of the position 5 deuterium of 5,6-D2-uridine to the proton of solvent, providing a −1
1031 Da mass shift [52].

1032

1033 *Internal standard RNAs and SILNAS-based quantitation of the stoichiometry of post-*
1034 *transcriptional modification*

1035 To construct the plasmids for i*n vitro* transcription of internal standard RNAs, DNAs encoding
1036 human 12S and 16S rRNAs were amplified by PCR from the mitochondrial DNA from TK6
1037 cells. The PCR primers used are as follows: HindIII-12S-Forward
1038 TATAAAGCTTAATAGGTTTGGTCCTAGCCTTTCTATTAGC, 12S-*Bam*HI-reverse
1039 ATATGGATCCGTTCGTCCAAGTGCACTTTCCAGTACACTT, *Hind*III-16S-forward
1040 TATAAAGCTTGCTAAACCTAGCCCCAAACCCACTCCACCT and 16S-*Xho*I-reverse
1041 ATATCTCGAGAAACCCTGTTCTTGGGTGGGTGTGGGTATA). The amplified DNAs were
1042 inserted into the multiple cloning sites of plasmid pCDNA3.1 (+) (Thermo Fisher Scientific). To
1043 synthesize RNA, 2 µg of template DNA was incubated and transcribed using Megascript T7 kit
1044 (Thermo Fisher Scientific). When RNA was synthesized, guanosine-$^{13}C_{10}$ 5′-triphosphate,
1045 cytidine-$^{13}C_9$ 5′-triphosphate, or uridine-$^{13}C_9$ 5′-triphosphate solution was used instead of the
1046 respective 5′-triphosphate reagent that contained carbons with a natural isotope distribution. The
1047 RNA was precipitated in ethanol, solubilized in nuclease-free water, and purified further by
1048 reversed-phase LC as described above.

1049 SILNAS-based quantitation was performed as described [90]. In brief, RNA (~100 fmol) from
1050 natural sources or cells grown in guanosine with natural isotope distribution was mixed with an
1051 equal amount of synthetic RNA transcribed *in vitro* with ^{13}C-labeled guanosine and digested
1052 with RNAse T1 (2 ng/µl). For the RNA transcribed with $^{13}C_9$-labeled cytidine and uridine, Rnase
1053 A (0.5 ng/µl) was used as the digestion enzyme. Digestion was carried out in 100 mM TEAA
1054 (pH 7.0) at 37°C. The 1:1 RNA mixing was performed based on the measurement of the

1055 absorbance at 260 nm and ensured later by a correction factor obtained experimentally. After
1056 obtaining the LC-MS spectrum of the digested RNA mixture, the stoichiometry of RNA
1057 modification at each site was estimated by Ariadne program designed for SILNAS [90]. The results
1058 were confirmed by manual inspection of the original MS spectrum to examine whether the
1059 estimates are based on 'uncontaminated' MS signals.

1060

1061 *Other procedures for RNA analysis*

1062 The masses of RNA fragments and a-, c-, w-, and y-series ions were calculated with Ariadne
1063 (http://ariadne.riken.jp/). Sequence-specific Rnase H cleavage of rRNAs was performed as
1064 described [91], using O-methylated RNA/DNA hybrid oligonucleotide complementary to the 12S
1065 and 16S rRNAs,
1066 GmUmUmCmGmUmCm(CAAG)UmGmCmAmCmUmUmUmCmCmAmGmUmAmCmAmC
1067 m and (AmAmCmCmCmUmGm(TTCT)UmGmGmGmUmGmGmGmUm, respectively (where
1068 Nm refers to 2'-O-methyl ribonucleotide and deoxyribonucleotides are indicated in parentheses).

1069

1070 <u>SDS-PAGE and immunoblotting analyses</u>

1071 Whole-cell protein extracts were obtained by solubilization in RIPA buffer (25mM Tris-HCl pH
1072 7.6, 150 mM NaCl, 1% NP-40, 1% sodium deoxycholate, and 0.1% SDS) with 1 mM PMSF and
1073 1x mammalian protease inhibitor. Extracts were cleared by 5 minutes of centrifugation at 10,000
1074 g at 4 °C. Protein concentrations were determined with the Folin phenol reagent. 40-60 µg of
1075 whole-cell protein extracts were separated by SDS-PAGE in the Laemmli buffer system.
1076 Proteins were then transferred to nitrocellulose membranes, subsequently blocked with 5% skim
1077 milk, and then incubated with antibodies against the indicated proteins followed by a second
1078 reaction with anti-mouse or anti-rabbit IgG conjugated to horseradish peroxidase. Signals were
1079 detected by chemiluminescence and exposure to X-ray films. For quantification, the signals in
1080 digitalized images were quantified by densitometry using the histogram function of Adobe
1081 Photoshop. Values were normalized to the signal of β-Actin and plotted as the percentage of WT
1082 using the Prism 8 software.

1083

1084 <u>Pulse labeling of mitochondrial translation products</u>

1085 Mitochondrial protein synthesis was determined by pulse-labeling of 60-70% confluent human
1086 wild-type (WT) HEK293T cells, *MRPS29*-KO HEK293T cells, and knockout cells stably
1087 reconstituted with mutant *MRPS29* variants. Cultures were grown in a medium without
1088 methionine and in the presence of 100 µg/mL emetine to inhibit cytoplasmic translation as
1089 described [92, 93]. Cells were labeled for 15 min at 37 °C with 100 µCi of ^{35}S-methionine
1090 (PerkinElmer Life Sciences, Boston, MA). After incubation, the medium containing ^{35}S-
1091 methionine was removed, the cells were washed once with PBS, and then the cells were
1092 incubated for 5 minutes in complete DMEM to allow recovery. After the short incubation, cells

1093 were washed once more with PBS, collected by trypsinization, and whole-cell protein extracts
1094 were obtained by solubilization with RIPA buffer. 40-50 µg of each sample was separated by
1095 SDS-PAGE on a 17.5% polyacrylamide gel, transferred to a nitrocellulose membrane, and
1096 exposed to X-ray film. Membranes were then probed by immunoblotting to assess the steady-
1097 state levels of β-ACTIN as a loading control. Values were normalized to the signal of β-ACTIN
1098 and plotted as the percentage of WT using the Prism 8 software. Potassium cyanide (KCN)-
1099 sensitive endogenous cell respiration was measured polarographically using a Clark electrode in
1100 the indicated cell lines. Cell respiration rates are presented as nmol of O_2 consumed per one
1101 million cells per minute.

1102

1103 Cryo-EM data acquisition

1104 Five cryo-EM datasets of mitoribosomal complexes were collected in total using EPU 1.9
1105 (Extended Data Table 1). First, 3 µL of ~120 nM mitoribosome was applied onto a glow-
1106 discharged (20 mA for 30 sec) holey-carbon grid (Quantifoil R2/2, copper, mesh 300) coated
1107 with continuous carbon (of ~3 nm thickness) and incubated for 30 sec in a controlled
1108 environment of 100% humidity and 4 ºC. The grids were blotted for 3 sec, followed by plunge-
1109 freezing in liquid ethane, using a Vitrobot MKIV (FEI/Thermofischer). For high resolution
1110 mitoribosome analysis, five separate datasets were collected on FEI Titan Krios
1111 (FEI/Thermofischer) transmission electron microscope operated at 300 keV, using C2 aperture of
1112 70 µm and a slit width of 20 eV on a GIF quantum energy filter (Gatan). A K2 Summit detector
1113 (Gatan) was used at a pixel size of 0.83 Å (magnification of 165,000X) with a dose of 29-32
1114 electrons/$Å^2$ fractionated over 20 frames. A defocus range of -0.6 to -2.8 µm was used. More
1115 detailed parameters for each one of the datasets are listed in Supplementary Table 1.

1116

1117 Cryo-EM data processing

1118 The complete workflows of the mitoribosomal complexes A/A-P/P-E/E, A/P-P/E, L1 stalk,
1119 monosome consensus map, SSU and their 8 masked regions are given in Extended Data Figs. 1
1120 and 2. For all the datasets, beam-induced motion correction and per-frame B-factor weighting
1121 were performed for all data sets using RELION-3.0.2 [36, 37]. Motion-corrected micrographs were
1122 used for contrast transfer function (CTF) estimation with gctf [94]. Unusable micrographs were
1123 removed by manual inspection of the micrographs and their respective calculated CTF
1124 parameters. Particles were picked in RELION-3.0.2 [36, 37] , using reference-free followed by
1125 reference-aided particle picking procedures. Reference-free 2D classification was carried out to
1126 sort useful particles from falsely picked objects, which were then subjected to 3D classification.
1127 3D classes corresponding to unaligned particles and LSU were discarded and monosome
1128 particles were pooled and used for 3D auto-refinement yielding a map with an overall resolution
1129 of 2.9-3.4 Å for the five datasets. Resolution was estimated using a Fourier Shell Correlation cut-
1130 off of 0.143 between the two reconstructed half maps. Finally, the selected particles were
1131 subjected to per-particle defocus estimation, beam-tilt correction and per-particle astigmatism

correction followed by Bayesian polishing. Bayesian polished particles were subjected to a second round per-particle defocus correction. A total of 994,919 particles from all datasets were then pooled and separated into 86 optics groups in RELION-3.1 [38], based on acquisition areas and date of data collection. Beam-tilt, magnification anisotropy and higher-order (trefoil and fourth-order) aberrations were corrected in RELION-3.1 [38]. Subsequently, 509,691 particles from datasets 2-4 were pooled together and subjected to 3D auto-refinement giving a final nominal resolution of 2.21 Å. Masked refinement was performed on the small subunit head, body, mS39 and tail to produce maps of 2.36 Å, 2.31 Å, 2.44 Å and 2.45 Å resolution, respectively and likewise for the SLU body, L10-L7/L12 stalk, CP and L1 stalk to yield maps of 2.08 Å, 2.38 Å, 2.36 Å and 2.89 Å resolution, respectively. To improve the quality of the L1-stalk map, 220,906 monosome particles with high occupancy of E/E-tRNA were pooled and subjected to partial signal subtraction using the mask that retains the E/E-tRNA and L1-stalk, followed by 3D auto-refinement to have a nominal resolution of 2.87 Å (Supplementary Fig. 1 and Supplementary Table 1).

For separating the A/A-P/P-E/E and A/P-P/E states, all 994,919 monosome particles were subjected to signal subtraction using the mask that retains the tRNA binding region. The tRNA binding sites displayed weak densities corresponding to a heterogeneous mixture of tRNAs bound with partial occupancy. Signal subtracted particles were 3D classified without alignment using a mask on the A-site. This yielded two main classes, one with density in the A-site (332,187 particles) and the other lacking it (629,597 particles). Particles with density in the A-site were selected and subjected to a second round of 3D-classification using a mask around the P- and E-sites. Two classes were selected, one with P/P- and E/E-tRNA density and other in hybrid state with P/E-tRNA density. All 3D classifications with signal subtracted particles were performed using a T-value of 400. The subtracted signal was reverted for these two classes, corresponding to the A/A-P/P-E/E state (82,522 particles) and A/P-P/E state (20,143 particles). Following 3D auto-refinement, the nominal resolution of the cosmplexes was 2.63 Å and 2.98 Å, respectively. Masked refinement for the classical state was performed using local masks on SSU head, body, tail, and mS39 to produce maps at 2.72 Å, 2.75 Å, 2.91 Å and 2.93 Å resolution, respectively. For the LSU body, L10-L7/L12, CP, and the L1 stalk regions, the resolution was 2.44 Å, 2.84 Å, 2.78 Å and 3.20 Å, respectively. Masked refinement for the hybrid state was performed using the same local masks as for the classical state but transformed to compensate for the structural differences. This produced maps for the SSU head, body, tail, and mS39 to produce maps of 3.03 Å, 3.07 Å, 3.39 Å and 3.47 Å resolution, respectively. For the LSU body, L10-L7/L12 region, CP, and the L1 stalk masks, the resolution was 2.84 Å, 3.29 Å, 3.25 Å and 3.53 Å, respectively. The maps were then subjected to modulation transfer function correction, automatic *B*-factor sharpening and local resolution filtering using RELION-3.1 (Supplementary Fig. 2, Supplementary Table 1).

1171 Model building and refinement

1172 We started by building a model into the 2.21 Å resolution consensus map. The starting model for
1173 the LSU was taken from PDB ID: 6ZSG, and for the SSU from PDB ID: 6RW4. These models
1174 were rigid body fitted using UCSF Chimera [95]. Individual local-masked refined maps with local-
1175 resolution filtering and *B*-factor sharpening (RELION 3.1) superposed to the overall map were
1176 combined into a single composite map using Phenix.combine_focused_maps [96] for model
1177 building and refinement. *Coot* v0.9 [97] with Ramachandran and torsion restraints was used for
1178 model building.

1179 The L1-stalk model was built using the 2.87 Å resolution masked-refined map of L1 stalk from
1180 E/E-tRNA-containing particles. Initial model for uL1m was generated by homology-modeling
1181 with uL1 structure of *T. thermophilus* (PDB ID: 3U4M) as template using the Swiss-Model
1182 webserver [98]. The N-terminal extension of uL1m (residues 61–93), the C-terminal domain
1183 (residues 158–254) and the preceding loop (residues 148–157) of uL9m, and H76-77 (residues
1184 2761–2786) of 16S rRNA were modeled manually into the density. Mitochondria-specific C-
1185 terminal extension of uL9m was modeled as a helix based on the density and secondary structure
1186 prediction by PSIPRED [99]. The model was rigid body fitted into the respective local-masked
1187 refined maps for L1 stalk region in the A/A P/P E/E and A/P/E states followed by self-restrained
1188 real space refinement in *Coot* v0.9.

1189 In the CP, the $tRNA^{Val}$ could be completely modeled, owing to the improved resolution of the
1190 local masked-refined map (2.36 Å). The 3′-CCA terminus (C74–A76) and a valine residue linked
1191 to A76 could be placed on the density map. The N-terminus of mL40 was extended by 13-
1192 residues (47–59) modeled in a tubular wedged between the A- and P-site tRNAs to the phosphate
1193 backbone of mRNA residue 7. Similarly, the C-terminus of bL31m was extended by 31 residues
1194 (95–125) from the C-terminal helix onto SSU head. The local resolution was sufficient for
1195 accurate side-chain modeling for most residues and secondary-structure assignments. We
1196 modeled a disulfide linkage between C45-C76 of mS37. However, they might exist in both
1197 disulfide-linked, and reduced states as indicated by the density and a water mediated hydrogen
1198 bond with a neighbouring Arginine side chain (R240 from uS7m). The other pair C55-C66
1199 appears to be reduced. However, as we had added 1mM DTT to our ribosome purification
1200 buffers, this is not truly indicative of the native state of C45-C76 or C55-C66 pairs.

1201 At the mRNA channel entrance, a more accurate and complete model of mS39 could be built
1202 with 29 residues added to the structure. Improved local resolution enabled unambiguous
1203 assignment of residues to the density which allowed us to address errors in the previous model.
1204 Finally, a total of 28 α-helices could be modeled in their correct register and orientation. Further,
1205 a 28-residue long N-terminal loop of mS31 (residues 247–275) along mS39 and mitochondria-
1206 specific N-terminal extension of uS9m (residues 53–70) approaching mRNA were modeled
1207 manually by fitting the loops into the density maps.

1208 Polyamines were identified upon a further manual inspection of the density map for the presence
1209 of continuous tubular densities which corresponded to spermine, spermidine or putrescine in

1210 length. A total of one spermine, four spermidines and one putrescine were placed in the model,
1211 justified by the electrostatic and hydrogen-bonding interactions that each polyamine exhibits at
1212 its amine groups with its neighbors.

1213 Metal ions, Mg^{2+}, K^{+} and Zn^{2+}, were modeled into densities based on a manual inspection of
1214 small density blobs and the chemical environment, specifically, coordination geometry and
1215 strength of density in both unsharpened and local resolution filtered maps. The coordination
1216 distance of Mg^{2+} is around 2 Å with an octahedral geometry, whereas that of K^{+} is around 3 Å
1217 with more relaxed constraints on coordination geometry. Notably, a density that was modeled
1218 previously as Zn^{2+} coordinated by residues D224, D240, D241 and H93 of uS2m was assigned as
1219 a magnesium ion, indicated by the octahedral geometry of coordination with the uS2m residues
1220 mentioned above and two water molecules.

1221 A-, P- and E-site tRNAs, and mRNA were modeled manually in the density. The density for
1222 tRNAs and mRNAs comes from a natively-bound heterogeneous population. Hence, individual
1223 residues were modeled as one of the nucleotides, A, U, G, or C, based on the density and/or
1224 conservation. While the 70 residues of P-site tRNA could be modeled, fewer residues could be
1225 modeled for the A-site (22 residues) and E-site tRNAs (43 residues), including the acceptor arm
1226 and anticodon loop due to weaker respective densities. Along the mRNA channel, 34 residues of
1227 mRNA were built. In the tRNA binding region, codon-anticodon pairs were clearly resolved.
1228 Additionally, extra residues near the A-site (10-12, 14-16) and at the mRNA channel entrance
1229 (25, 27-29) were modeled accurately into density. For the remaining mRNA chain at a relatively
1230 lower resolution, correct overall chain trace and nucleotide orientation could be assigned. This
1231 allowed specific protein-nucleotide interactions to be identified for uS5m, uS7m, uS9m, uS12m,
1232 mS35, mS39 and mL40.

1233 For modeling the classical A/A P/P E/E- and hybrid A/P P/E-states, the LSU and SSU from the
1234 consensus model were fitted into their composite maps, followed by manual revision. As
1235 described above, tRNAs and mRNA were modeled manually into the density.

1236 The water molecules were automatically picked by *Coot* v0.9 [62], followed by manual revision.
1237 Geometrical restraints of modified residues and ligands used for the refinement were calculated
1238 by Grade Web Server (http://grade.globalphasing.org) or obtained from CCP4 library [100].
1239 Hydrogens were added to the models except for water molecules by REFMAC5 [101] using the
1240 prepared geometrical restraint files. Charged α-amino-group hydrogens (H2 and H3) and a free-
1241 ribose hydrogen HO3′ were removed from non-terminal protein and RNA residues, respectively,
1242 while those at terminal residues were kept. Protonation of Histidine residues were judged based
1243 on the chemical environment and removed or kept their N-H hydrogens (HD1 and HE2)
1244 accordingly. Protonation/deprotonation of ligands and modified residues were also adjusted.

1245 Final models were further subjected to refinement with Phenix.real_space_refine v1.13_2998 [96],
1246 wherein three macro-cycles of global energy minimization with reference restraints (using the
1247 input model as the reference, sigma 5-7) and secondary structure restraints, rotamer restraints but
1248 without Ramachandran restraints were carried out for each model. The composite maps were

1249 used as the targets for the refinement. An 'edit' file that defines metal-coordination bonds was
1250 generated by ReadySet in the Phenix suite and used. Non-canonical covalent bonds, which are
1251 those between $tRNA^{Val}$ and Valine and between 1-methyl-isoaspartate 184 and G185 in uS11m,
1252 were also defined in the 'edit' file. Model refinement data are listed in Supplementary Table 1.

1253

1254 Bioinformatic analysis of the Y-N-C-Y motif

1255 The density and base-specific interactions of mRNA residues 25-28 with mS39 imply a sequence
1256 of pyrimidine, any nucleotide, cytosine, pyrimidine, leading to a consensus motif: Y-N-C-Y. We
1257 explored the possibility of increased frequency of this motif in mRNA sequences. The sequences
1258 for all 13 mRNAs were obtained from GenBank. The consensus motif was searched in each
1259 sequence and all occurrences (including ones that overlap) were recorded and used to calculate
1260 the percentage frequency of occurrence for each transcript and the average percentage frequency.
1261 To determine if there is an enrichment of this motif in mRNAs, we calculated its occurrence in a
1262 set of nuclear-encoded mRNAs. To create this set, we acquired sequences randomly from
1263 GenBank and subjected them to a 90% redundancy cut-off, resulting in a total of 1369
1264 sequences. The percentage frequency of occurrence of Y-N-C-Y motif was determined for each
1265 of the 1370 sequences and used to calculate an average percentage frequency for the entire set.
1266 Next to determine the distribution of the Y-N-C-Y motif across the length of mRNAs, each
1267 occurrence was plotted against its position number in the mRNA sequence. This distribution for
1268 all 13 mRNA sequences was plotted together for comparison.

1269

1270 Molecular Dynamics simulations: Modified force fields for simulating a truncated mL64 protein
1271 and modified interactions with protein uL1m

1272 *Baseline force field used for simulations of P/E formation*

1273 An all-atom multi-basin structure-based "SMOG" model [60, 61] of the mitoribosome was used to
1274 simulate P/E formation. For this, we first constructed single-basin structure-based models for the
1275 pre- and post-translocation configurations (A/A-P/P and P/P-E/E). We then combined the two
1276 models, such that the composite model stabilizes both the pre- and post-translocation
1277 configurations. Here we describe the baseline model, which is described in the main text. In
1278 subsequent sections, we provide detailed descriptions of all modified force fields.

In a single-basin all-atom structure-based model, every non-hydrogen atom is represented by a bead of unit mass, and an experimentally-obtained structure is used to define the potential energy minimum. The functional form of the potential is given by:

$$U = \sum_{\text{bonds}} \frac{\epsilon_r}{2}(r_i - r_{i,0})^2 + \sum_{\text{angles}} \frac{\epsilon_\theta}{2}(\theta_i - \theta_{i,0})^2$$

$$+ \sum_{\text{impropers}} \frac{\epsilon_{\chi_{imp}}}{2}(\chi_i - \chi_{i,0})^2 + \sum_{\text{planars}} \epsilon_{\chi_{planar}}[1 - \cos(2\chi_i)]$$

$$+ \sum_{\substack{\text{backbone}\\\text{dihedrals}}} \epsilon_{bb} F(\phi_i - \phi_{i,0}) + \sum_{\substack{\text{sidechain}\\\text{dihedrals}}} \epsilon_{sc} F(\phi_i - \phi_{i,0})$$

$$+ \sum_{\text{contacts}} \epsilon_c \left[\left(\frac{\sigma_{ij}}{r_{ij}}\right)^{12} - 2\left(\frac{\sigma_{ij}}{r_{ij}}\right)^{6} \right] + \sum_{\text{non-contacts}} \epsilon_{nc} \left(\frac{\sigma_{nc}}{r_{ij}}\right)^{12}$$

where

$$F(\phi) = [1 - \cos(\phi)] + \frac{1}{2}[1 - \cos(3\phi)]$$

r_0 and θ_0 parameters are assigned values found in the Amber ff03 force field [102]. The dihedral parameters ϕ_0 are defined by the experimental structure. χ_0 non-planar improper dihedrals (around chiral centers) are also defined to have the values adopted in the experimental structures. Planar dihedral angles are given a cosine term with periodicity 2 and minima at 0 and 180 degrees. The energy scale is set to $\epsilon_r = 100\frac{\epsilon}{A^2}, \epsilon_\theta = 80\frac{\epsilon}{rad^2}, \epsilon_{\chi_{imp}} = 10\frac{\epsilon}{rad^2}, \epsilon_{\chi_{planar}} = 40\frac{\epsilon}{rad^2}$, where ϵ is the reduced energy scale. The dihedral and contact energy scales $\epsilon_{bb}, \epsilon_{sc}, \epsilon_C$ are normalized as in Ref. [60].This combination of structure-based non-bonded terms and AMBER bonded terms is identical to the implementation of a previous SMOG-amber variant (called SBM_AA-amber-bonds [103] in the SMOG 2 force field repository (smog-server.org), though post-transcriptionally-modified residues were added for the current model. Upon publication, the SMOG 2 force field templates used in the current study will be available for download on the SMOG 2 force field repository (ID: AA_PTM_Hassan21.v1).

For the non-bonded interactions, each atomic contact that is found in the experimental structure (i.e. "native'' contact) is given an attractive Lennard-Jones-like interaction that stabilizes a preassigned structure. Native contacts were defined based on the Shadow Contact Map algorithm with default parameters [104]. Σ_{ij} are the interatomic distances between contacts in the native structure, multiplied by 0.96. As employed previously in simulations of the ribosome [105, 106] and viral capsids [103], this scaling of the contact distance was employed to avoid artificial expansion of the ribosome that results from thermal energy. That is, while the potential energy is defined such that the experimental structure is the global minimum, thermal energy leads to a free-energy minimum for which the ribosome is slightly expanded. By shortening the stabilizing interactions, the free-energy minimum is consistent with the experimental structure. For this comparison, the radius of gyration (R_g) was used as a measure of expansion. With this scaling of the contact

distances, R_g was found to match that of the cryo-EM model. All non-native contacts are given a repulsive term that ensures excluded-volume steric interactions are present. The parameter σ_{nc} is given the value 2.5 Å, while $\epsilon_{nc} = 0.1\epsilon$.

Stabilizing intra-ribosome contacts and dihedrals were assigned the values found in the A/P-P/E (SSU rotated) hybrid structure, which is described in the main text. This ensures that the SSU rotates forward in each simulation. Each simulation is initiated from the A/A-P/P conformation. All intra-mt-tRNA and intra-mt-mRNA contacts were defined based on the A/A-P/P structure. Since stabilizing contacts in a structure-based model describe effective interactions [107, 108], we rescaled the strengths of subsets of contacts within the model. Consistent with recent simulations of P/E formation in bacteria [105], interactions that stabilize the structure of the ribosome (i.e. intra-ribosomal) are given larger weights than contacts that are only transiently-formed (e.g. tRNA-ribosome contacts). Relative to intra-ribosome contacts, the energetic interactions between the mt-mRNA-tRNA complex and the SSU (in A/A-P/P and P/P-E/E structures) were rescaled by a factor of 0.3. While these interactions were weaker than intra-ribosomal contacts, since the simulations were not performed under conditions in which translocation will occur (*e.g.*, binding of elongation factors or back-rotation, etc), the mt-mRNA maintained its initial position on the mRNA track of the SSU. P/P-E/E contacts between the mt-tRNA and the uL1m protein were rescaled by a factor of 0.8 and all other interactions between mt-mRNA-tRNA and the LSU were rescaled by a factor of 0.1. This rescaling was applied to account for the transient nature of mt-mRNA-tRNA binding to the ribosome. The strength of the uL1m-tRNA contacts was set such that the P/E configuration would stably form contacts with the uL1m protein. When contacts were scaled below a factor of ~0.5, we found that uL1m could not form stable interactions with the mt-tRNA.

Interactions between the 3′-CCA ends of A-site and P-site mt-tRNAs with the A-site and the P-site were scaled by a factor of 0.2, while their interactions with P-site and E-site were scaled by a factor of 0.8. This leads to the mt-tRNA molecules favoring binding of their target sites (*i.e.*, sites bound in the P/E configuration) on the ribosome. While the interactions with the subsequent binding site (*i.e.*, A-site mt-tRNA with the P-site and P-site mt-tRNA with the E-site) were stronger, these contacts are short range (~6 Å). Accordingly, the stronger weights do not affect the dynamics of the mt-tRNA until it is very close to the binding site. Thus, the details of the final repositioning of the 3′-CCA tail of the P-site mt-tRNA should not be overinterpreted. While the contacts are short-range, the structure of the mitoribosome may introduce steric barriers that the mt-tRNA must navigate in order to adopt the P/E configuration [108]. With these considerations in mind, the current model is aimed at identifying structural elements that can impose steric limitations on mt-tRNA during P/E formation.

There were also two sets of harmonic potentials that were introduced. To mimic the presence of a nascent peptide chain, which would restrain the 3′-CCA end of the A-site tRNA to the PTC, we introduced weak harmonic restraints (weight of $1/nm^2$) between the 3′-CCA end of the A-site tRNA and the P site of the LSU. Distances were assigned based on the P/P conformation. These weak interactions ensured that the 3′-CCA end remains localized to the PTC. We also

introduced harmonic potentials between base-pairing contacts in the mt-tRNA acceptor arm (weight 1000/nm^2). Due to the details of the contact map, initial simulations exhibited partial unfolding/refolding of the acceptor arm during P/E formation. Since that was likely an artifact due to the simplicity of the model and the details of the contact map definition, these additional harmonic terms were introduced to ensure the tRNA acceptor arm remained folded throughout the transition.

Modified force fields

Multiple variants of the model (*i.e.*, force field) were considered, in order to investigate the influence of steric interactions between the P-site mt-tRNA and C-terminal residues of mL64 and to investigate the influence of attractive interactions between uL1m and P-site mt-tRNA on P/E formation.

Truncated-mL64 model: ΔmL64 force field

The C-terminal region of mL64 is involved in steric interactions with the mt-tRNA. For ΔmL64 model, the C-terminal region of mL64 (beginning with Q112) was removed from the system. Q112 was chosen as truncating here guarantees no steric interactions between mL64 and the mt-tRNA and keeps the rest of the protein intact. Thus, all other interactions were unperturbed. This model is intended to mimic an ideal experiment, where one could delete the terminal region of mL64 without introducing indirect effects on the dynamics. In our application, this model allows us to ask what effect steric interactions between P-site mt-tRNA elbow and mL64 have on the dynamics of P/E formation. Deletion of this region from the model was achieved using the smog_extract tool of the SMOG 2 software package [60].

Modified-uL1m model: ΔuL1m force field

All stabilizing contacts between uL1m and the P-site mt-tRNA that are formed in the P/P-E/E state were scaled by a relative factor of 0.1, rather than 0.8 (baseline model, above). Thus, by weakening the attractive interactions, there is insufficient stabilizing energy between uL1m and the P/E tRNA, such that the tRNA elbow does not fully reach the P/E configuration.

Combined truncated mL64 and modified uL1m model: ΔmL64-ΔuL1m force field

All modifications applied in the truncated mL64 model and the modified-uL1m model were included in a single combined force field.

Simulation details

All simulations were initiated from the pre-translocation A/A-P/P configuration. All force field files were generated using the SMOG 2 software package [60]. Molecular dynamics simulations

1382 were performed using Gromacs (v5.1.4) [109, 110]. Reduced units were used in all calculations.
1383 Energy minimization was first performed using steepest descent minimization. The system was
1384 then coupled to a heat bath using Langevin Dynamics protocols, with reference temperature of
1385 0.5 ε/k_B reduced temperature units (60 Gromacs units). This temperature was chosen since it has
1386 been shown to produce structural fluctuations that are consistent with those inferred from
1387 anisotropic *B*-factors and explicit-solvent simulation [111]. The timestep was 0.002 reduced units
1388 and each simulation was continued until the distance of the 3'-CCA end from the LSU E-site
1389 R_{CCA} reached a value less than 4 Å. Energy minimization was initially performed using steepest
1390 descent minimization. Each simulation was performed for a maximum of 10^8 timesteps. For the
1391 primary/baseline model described in the main text (327 simulations) we obtained an aggregate
1392 simulated time of 2.27 $*10^6$ reduced units. For the truncated mL64 model (ΔmL64 model) (321
1393 simulations), the aggregate simulation time was 1.87 $*10^6$ reduced units. For the attenuated uL1m
1394 contacts model (ΔuL1m model) (237 simulations), the aggregate simulation time was 1.76 $*10^6$
1395 reduced units. For the ΔmL64-ΔuL1m model (181 simulations), the aggregate simulation time
1396 was 1.04 * 10^6. Previous comparisons of diffusion coefficients of tRNA molecules in the
1397 ribosome (explicit-solvent simulations vs. SMOG models), estimate that 1 reduced unit
1398 corresponds to an effective timescale of approximately 1 nanosecond [112]. Using this conversion
1399 factor, the presented simulations represent an aggregate effective simulate time of ~ 6.94
1400 milliseconds.

1401 *Structural metrics for describing simulated dynamics*

1402 - A-site mt-tRNA, R^P_{CCA}: distance between the geometric centers of the side chains of C75 in the
1403 A-site mt-tRNA and Gm2815 in the LSU rRNA. These residues base pair in the A/P-P/E and
1404 P/P-E/E configurations.

1405 - P-site mt-tRNA, R^P_{CCA}: distance between the geometric centers of the side chains of C75 in the
1406 P-site mt-tRNA and Gm2815 in the LSU rRNA. These residues base pair in the A/P-P/E
1407 configuration.

1408 -R_{CCA}: distance between the geometric centers of the side chains of A76 in the P-site mt-tRNA
1409 and G2909 in the LSU rRNA. G2909 in the E-site forms a base stacking interaction with A76 of
1410 P-site mt-tRNA in the A/P-P/E configuration.

1411 -R_{elbow}: distance between geometric centers of U54 of P-site mt-tRNA and its reference position
1412 in the A/P-P/E configuration after alignment of the LSU rRNA.

1413 - $Q_{\mathrm{L1-tRNA}}$: the fraction of P/P-E/E contacts between uL1m and P-site mt-tRNA. A contact is
1414 defined as formed if it is within a factor of 1.2 of the distance found in the P/P-E/E configuration.

1415

1416 *SSU rotation and tilt angles*

1417 To follow the rotary motions of the SSU body with respect to the LSU, we calculated rotation
1418 and tilt angles for both the SSU body. For this, we first determined the corresponding *E. coli*
1419 numbering of the mitoribosome rRNA residues via STAMP alignment [113] of the mitoribosome to

1420 a reference *E. coli* structure (PDB ID: 4V9D). Alignment was performed separately for the LSU,
1421 SSU head and SSU body. The angles were then calculated, using the assigned *E. coli* numbering.
1422
1423 *Structural model preparation for simulations*
1424 Since the cryo-EM models did not resolve the exact same set of atoms, there was a need to
1425 perform some additional structural models prior to performing simulations. For example, to
1426 define the multi-basin structure-based model, it was necessary for each mt-tRNA molecule to
1427 have identical atoms in the pre- and post-translocation configurations. Additionally, to define
1428 the intra-ribosome interactions to stabilize the A/P-P/E conformation, it was necessary that all
1429 mt-rRNA and mitoribosomal proteins had identical atomic composition. While most of the
1430 resolved atoms are common to all reported models, we employed restraint-based modeling to
1431 construct models of the mitoribosome and mt-tRNA that have identical compositions. Below, we
1432 describe the steps required for modeling the mitoribosome and mt-tRNA.
1433
1434 *Structural modeling pre-processing steps for rRNA and proteins for simulations*
1435 Since the structure-based model only included intra-ribosome interactions from the A/P-P/E
1436 structure, we first removed all mt-tRNA and mt-mRNA from the A/A-P/P and A/P-P/E models.
1437 We also removed ligands and water molecules (HOH, SPD, PUT, NAD, SPM). For the
1438 remaining atoms, we identified all atoms that were common to the A/A-P/P and A/P-P/E
1439 structures. We then generated a single-basin structure-based model of the A/A-P/P structure.
1440 Next, position restraints (harmonic terms, weight of 100 for each atom) were introduced for all
1441 common atoms, with positions corresponding to the A/P-P/E structure. The system was then
1442 energy minimized via steepest descent minimization. Then, the system was subject to simulated
1443 annealing. The system was initially simulated at 0.15 reduced temperature units for 25,000
1444 timesteps. The temperature was then linearly decreased to 0 over the next 50,000 timesteps. An
1445 additional 25,000 steps were simulated at temperature 0. The final, annealed structural model
1446 was used for force field generation steps, as described above.
1447
1448 *Structural modeling pre-processing steps for mt-tRNA and mt-mRNA*
1449 Since the cryo-EM reconstructions reported consensus/average sequences for each mt-tRNA, the
1450 composition of the A-, P- and E-site mt-tRNAs were not identical. To perform simulations, we
1451 homogenized the composition of the mt-tRNA molecules in the A/A-P/P-E/E structure and the
1452 mt-tRNA codons. For this, we started with the structural model of the A-site mt-tRNA (and the
1453 associated codon) from the A/A-P/P structure, and then used it to generate a structure-based
1454 model. We then introduced position restraints based on the positions of the A-site mt-tRNA in
1455 the A/A-P/P-E/E structure. All common atoms (*i.e.*, backbone atoms, or atoms in identical
1456 residues) were restrained to the A-site mt-tRNA/mRNA positions. For the A-site mt-tRNA,
1457 restraints were not imposed on residues 46-58 and 16-17. Cycles of minimization and annealing

1458 were performed, where the position restraints were given weights of 1, 10, 100 and then 1000.
1459 This process was repeated for the P-site and E-site mt-tRNAs, as well as for the upstream and
1460 downstream mt-mRNA. This process produced a model of the A/A-P/P-E/E configuration that
1461 has repeating codons and identical mt-tRNA composition. This structural model was used to
1462 define the pre-translocation and post-translocation structure-based models, which were used to
1463 construct the multi-basin model.

1464 *Describing the sequence of rearrangements in simulations*

1465 To describe the dynamics of the P-site mt-tRNA during P/E state formation, we have defined
1466 three states based on the 2D probability distribution of R^E_{elbow} and R^E_{CCA} distances (Fig. 8). These
1467 states are defined as all configurations of the P-site mt-tRNA in the baseline model that sample
1468 the following values of R^E_{elbow} & R^E_{CCA}:
1469 state I_1: disk centered at (R^E_{elbow},R^E_{CCA})=(46,35) Å with radius r=6 Å
1470 state I_2: disk centered at (R^E_{elbow},R^E_{CCA})=(63,23) Å with radius r=8 Å
1471 state I_3: disk centered at (R^E_{elbow},R^E_{CCA})=(42,13) Å with radius r=7 Å
1472
1473 Using this definition of the intermediate states, the most common sequence of transitions
1474 followed the order P/P => I_1 => I_2 => I_3 => P/E.
1475

1476 Structure analysis and Fig.s

1477 Visualization and analysis of the models and maps was carried out using UCSF Chimera and
1478 ChimeraX [95, 114]. For model and map comparisons, models were superposed in *Coot* v0.9 [62] using
1479 the Secondary Structure Matching algorithm and maps downloaded from EMDB were resampled
1480 on our maps in UCSF Chimera. Simulated snapshots were visualized using Visual Molecular
1481 Dynamics [115].

1482

1483 Quantitation and statistical analysis

1484 All experiments were done in at least biological triplicate unless otherwise stated. GraphPad
1485 Prism 8 software was used for statistical analyses of the data. One-way analysis of variance
1486 (ANOVA) was performed, comparing the mean of each cell line with the mean of the mS29-KO
1487 cell line reconstituted with WT mS29, followed by Dunnett's multiple comparisons test. The
1488 data is presented as the mean ± SD; * $P \leq 0.05$, ** $P \leq 0.01$, *** $P \leq 0.001$, **** $P \leq 0.0001$. For
1489 immunoblotting, band density is quantified and normalized to ACTIN. For metabolic labeling of
1490 mitochondrially translated peptides in whole cells, the data presented represents the mean of each
1491 sample's ^{35}S signals.

1492

1493 **Additional References**

1494 86. Aibara S, Andrell J, Singh V, Amunts A. Rapid Isolation of the Mitoribosome from HEK
1495 Cells. *J Vis Exp*, (2018).

1496
1497 87. Morita E, Arii J, Christensen D, Votteler J, Sundquist WI. Attenuated protein expression
1498 vectors for use in siRNA rescue experiments. *Biotechniques* **0**, 1-5 (2012).
1499
1500 88. Yamauchi Y*, et al.* Denaturing reversed phase liquid chromatographic separation of non-
1501 coding ribonucleic acids on macro-porous polystyrene-divinylbenzene resins. *J*
1502 *Chromatogr A* **1312**, 87-92 (2013).
1503
1504 89. Nakayama H, Yamauchi Y, Taoka M, Isobe T. Direct identification of human cellular
1505 microRNAs by nanoflow liquid chromatography-high-resolution tandem mass
1506 spectrometry and database searching. *Anal Chem* **87**, 2884-2891 (2015).
1507
1508 90. Taoka M*, et al.* Landscape of the complete RNA chemical modifications in the human
1509 80S ribosome. *Nucleic Acids Res* **46**, 9289-9298 (2018).
1510
1511 91. Taoka M*, et al.* The complete chemical structure of Saccharomyces cerevisiae rRNA:
1512 partial pseudouridylation of U2345 in 25S rRNA by snoRNA snR9. *Nucleic Acids Res*
1513 **44**, 8951-8961 (2016).
1514
1515 92. Bourens M, Barrientos A. A CMC1-knockout reveals translation-independent control of
1516 human mitochondrial complex IV biogenesis. *EMBO Rep* **18**, 477-494 (2017).
1517
1518 93. Leary SC, Sasarman F. Oxidative phosphorylation: synthesis of mitochondrially encoded
1519 proteins and assembly of individual structural subunits into functional holoenzyme
1520 complexes. *Methods Mol Biol* **554**, 143-162 (2009).
1521
1522 94. Zhang K. Gctf: Real-time CTF determination and correction. *J Struct Biol* **193**, 1-12
1523 (2016).
1524
1525 95. Pettersen EF*, et al.* UCSF Chimera--a visualization system for exploratory research and
1526 analysis. *J Comput Chem* **25**, 1605-1612 (2004).
1527
1528 96. Afonine PV*, et al.* Real-space refinement in PHENIX for cryo-EM and crystallography.
1529 *Acta Crystallogr D Struct Biol* **74**, 531-544 (2018).
1530
1531 97. Emsley P, Cowtan K. Coot: model-building tools for molecular graphics. *Acta*
1532 *Crystallogr D Biol Crystallogr* **60**, 2126-2132 (2004).
1533
1534 98. Waterhouse A*, et al.* SWISS-MODEL: homology modelling of protein structures and
1535 complexes. *Nucleic Acids Res* **46**, W296-W303 (2018).
1536
1537 99. Buchan DWA, Jones DT. The PSIPRED Protein Analysis Workbench: 20 years on.
1538 *Nucleic Acids Res* **47**, W402-W407 (2019).
1539

100. Krissinel EB, *et al.* The new CCP4 Coordinate Library as a toolkit for the design of coordinate-related applications in protein crystallography. *Acta Crystallogr D Biol Crystallogr* **60**, 2250-2255 (2004).

101. Murshudov GN, *et al.* REFMAC5 for the refinement of macromolecular crystal structures. *Acta Crystallogr D Biol Crystallogr* **67**, 355-367 (2011).

102. Duan Y, *et al.* A point-charge force field for molecular mechanics simulations of proteins based on condensed-phase quantum mechanical calculations. *J Comput Chem* **24**, 1999-2012 (2003).

103. Whitford PC, Jiang W, Serwer P. Simulations of Phage T7 Capsid Expansion Reveal the Role of Molecular Sterics on Dynamics. *Viruses* **12**, (2020).

104. Noel JK, Whitford PC, Onuchic JN. The shadow map: a general contact definition for capturing the dynamics of biomolecular folding and function. *J Phys Chem B* **116**, 8692-8702 (2012).

105. Levi M, Walak K, Wang A, Mohanty U, Whitford PC. A steric gate controls P/E hybrid-state formation of tRNA on the ribosome. *Nat Commun* **11**, 5706 (2020).

106. Nguyen K, Whitford PC. Steric interactions lead to collective tilting motion in the ribosome during mRNA-tRNA translocation. *Nat Commun* **7**, 10586 (2016).

107. Chan HS, Zhang Z, Wallin S, Liu Z. Cooperativity, local-nonlocal coupling, and nonnative interactions: principles of protein folding from coarse-grained models. *Annu Rev Phys Chem* **62**, 301-326 (2011).

108. Levi M, Noel JK, Whitford PC. Studying ribosome dynamics with simplified models. *Methods* **162-163**, 128-140 (2019).

109. Hess B, Kutzner C, van der Spoel D, Lindahl E. GROMACS 4: Algorithms for Highly Efficient, Load-Balanced, and Scalable Molecular Simulation. *J Chem Theory Comput* **4**, 435-447 (2008).

110. Lindahl E, Hess B, van der Spoel D. GROMACS 3.0: a package for molecular simulation and trajectory analysis. *Journal of Molecular Modeling* **7**, 306-317 (2001).

111. Jackson J, Nguyen K, Whitford PC. Exploring the balance between folding and functional dynamics in proteins and RNA. *Int J Mol Sci* **16**, 6868-6889 (2015).

112. Yang H, Bandarkar P, Horne R, Leite VBP, Chahine J, Whitford PC. Diffusion of tRNA inside the ribosome is position-dependent. *J Chem Phys* **151**, 085102 (2019).

113. Russell RB, Barton GJ. Multiple protein sequence alignment from tertiary structure comparison: assignment of global and residue confidence levels. *Proteins* **14**, 309-323 (1992).

114. Pettersen EF*, et al.* UCSF ChimeraX: Structure visualization for researchers, educators, and developers. *Protein Sci* **30**, 70-82 (2021).

115. Humphrey W, Dalke A, Schulten K. VMD: visual molecular dynamics. *J Mol Graph* **14**, 33-38, 27-38 (1996).

Data availability statement

The atomic coordinates were deposited in the RCSB Protein Data Bank, and EM maps have been deposited in the Electron Microscopy Data bank under accession numbers: 7QI4 and EMD-13980 (consensus monosome), 7QI5 and EMD-13981(classical state), 7QI6 and EMD-13982 (hybrid state).

The atomic coordinates that were used in this study: 3U4M (uL1 from *T. thermophilus*), 4V51 (*T. thermophilus* ribosome with mRNA, tRNA), 4V9D (*E. coli* ribosome), 4Y4P (*T. thermophilus* ribosome with A-, P-, E-site tRNAs), 6QNR (*T. thermophilus* ribosome with experimentally assigned K^+ ions) 6RW4 (mtSSU with mtIF3), 6ZM5 (mitoribosome from actinonin-treated cells) 6ZSG (mitoribosome with mRNA, tRNA), 6ZTJ (*E.coli* expressome), 6ZTN (*E.coli* expressome), 7K00 (*E. coli* ribosome at 2 Å resolution).

Acknowledgments

We thank the EMBO Young Investigator Program, the Northeastern University Discovery cluster and Northeastern University Research Computing staff. Swedish Foundation for Strategic Research (FFL15:0325), Ragnar Söderberg Foundation (M44/16), European Research Council (ERC-2018-StG-805230), Knut and Alice Wallenberg Foundation (2018.0080), Japan Science and Technology Agency (19198049), NIH-R35 grant (GM118141 to A.B.), and MDA Research Grant (MDA-381828 to A.B.). V.S. is supported by the Horizon 2020 - Marie Sklodowska-Curie Innovative Training Network (721757). Y.I. was supported by H2020-MSCA-IF-2017 (799399-Itohribo). The SciLifeLab cryo-EM facility is funded by the Knut and Alice Wallenberg, Family Erling Persson, and Kempe foundations. P.C.W. was supported by NSF grant MCB-1915843. Work at the Center for Theoretical Biological Physics was also supported by the NSF (Grant PHY-2019745). We would like to thank AMD for the donation of critical hardware and support resources from its HPC Fund that made this work possible.

Author contributions

V.S., Y.I., S.A., and J.A. collected cryo-EM data. V.S. and Y.I. processed the data and built the models. V.S., Y.I., R.K.F., A.N., S.A. and A.A. carried out structural analysis. Y.N., K.I. and M.T. performed mass-spec characterization. S.L.D. and A.B. performed biochemical characterization. A.H. and P.C.W. performed molecular simulations. All authors contributed to data interpretation and manuscript writing.

Competing Interests Statement

The authors declare no competing interests.